

3D-Printed Microstrip Resonators for 4.7T MRI

by

Saeed Javidmehr

A thesis submitted in partial fulfillment of the requirements for the degree of

Master of Science

in

Electromagnetics and Microwaves

Department of Electrical and Computer Engineering  
University of Alberta

© Saeed Javidmehr, 2015

## **Abstract**

Radiofrequency (RF) coils are a substantial part of Magnetic Resonance Imaging System. Microstrip transmission line (MTL) coils are widely used as they have a low coupling between array elements and negligible radiation loss. Matching and tuning capacitors are usually soldered to MTL coils in order to tune them to Larmor frequency and match them to  $50\Omega$ . Typically, these coils need to be adjusted according to different sample loadings (patients) in MRI. Availability and high cost of MR compatible variable or fixed capacitors for tuning and matching and the labour-intensive work encourage us to find an easy way to satisfy these requirements with low cost and less process steps.

Here, we propose to use rapid prototyping (additive manufacturing), such as 3D printing, to overcome the existing problems and print MRI coils all at once including the matching/tuning capacitors. Additive Manufacturing is an emerging manufacturing technology that offers new prototyping and fabrication methods to RF world. Additive manufacturing technology could potentially grant reduction of fabrications steps for MTL coils. A typical desktop 3D printer is capable of printing only plastics, such as ABS and PLA. Moreover, there is no low cost 3D printer to provide metal and plastic printing in one machine. In this thesis, a low cost desktop 3D printer has been modified to add ink printing capability.

In addition, the design procedure of MTL coils with parallel plate capacitors as matching and tuning capacitors is reported. 3D printing as a new technology is adopted to fabricate the MTL coils. The MTL coils with built-in parallel plate capacitors from plastic materials and two different conductive materials (copper

tape and silver ink) are designed and fabricated for 4.7 T MRI systems. Moreover, the fabricated coil's performance in terms of quality factor and SNR is investigated.

Based on the results of this thesis, 3D printing technology provided faster prototyping process for MRI coils. It also allowed design iterations to increase the coil's performance in MRI. 3D-printed parallel plate capacitors integrated with MTL coils eliminated the repetitive work of soldering, and mitigated the process for iterations during measurements. Thermoplastic material such as ABS and PLA showed comparable SNR and efficiency values to standard low loss foam, and therefore they can be used in MR applications. Ink-printed MTL coils showed lower performance compared to low loss foam, and that can be attributed to the ink conductivity.

## **Acknowledgments**

To begin, I would like to acknowledge and say thank you to my parents Yaghoob Javidmehr and Simin Nasehy. I cherish them and am grateful for their constant love and support in my life. They have provided me with many opportunities and have always encouraged my educational pursuits. They have loved me and have been a source of strength and stability that I could rely upon. I dedicate this thesis to them.

I gratefully acknowledge Prof. Mojgan Daneshmand and Prof. Nicola De Zanche; both have been true leaders and have played pivotal roles as my supervisors throughout this work.

Here too, I acknowledge my colleague Adam Maunder who has helped make this work possible. His encouragement and best wishes have been a tremendous support to me. I would also like to thank Peter Seres for his assistance in imaging. As well, I would like to thank my colleague Sabreen Khan for her assistance in proofreading this thesis.

I would also like to thank the Natural Sciences and Engineering Research Council of Canada (NSERC) for funding this project.

# Table of Contents

Abstract.....	ii
Acknowledgments.....	iv
Table of Contents.....	v
List of Tables.....	viii
List of Figures.....	ix
List of Abbreviations.....	xii
Chapter 1 Introduction.....	1
1.1 Background.....	1
1.2 Motivation and Objective.....	2
1.3 Thesis Structure.....	3
Chapter 2 MRI Theory.....	5
2.1 Relaxation.....	10
2.2 Signal Detection.....	11
2.3 Spatial Encoding and Gradients.....	12
2.4 Image Contrast.....	16
2.4.1 Inversion Recovery Sequence.....	16
2.4.2 Spin Echo Sequence.....	17
2.4.3 Gradient Echo.....	18
Chapter 3 Literature Review.....	19
3.1 RF Coils.....	19
3.1.1 Transmit Arrays.....	21
3.1.2 Volume Coils.....	22
3.1.3 Conductors and the Skin Effect.....	22

3.1.4	Coil Conductivity Loss .....	23
3.1.5	Birdcage Coil Frequency Tuning and Impedance Matching .....	24
3.1.6	Microstrip Coils .....	24
3.1.7	Performance Evaluation.....	28
3.1.8	Transmit Efficiency and Loss .....	29
3.1.9	Radiation Losses .....	30
3.1.10	Homogeneity.....	30
3.1.11	Dielectric Losses from Sample .....	31
3.1.12	Sample Inductive Loss .....	33
3.1.13	Signal to Noise Ratio .....	33
3.1.14	RF Coil's Quality Factor.....	34
3.1.15	Methods for Measuring Q.....	36
3.2	Additive Manufacturing .....	37
3.2.1	Photopolymer-based Systems: .....	38
3.2.2	Powder-based Systems: .....	38
3.2.3	Molten Material Systems: .....	39
3.2.4	Technology Overview.....	42
3.2.5	Material Properties.....	42
3.2.6	Challenges.....	45
3.2.7	Shortcomings and Objectives .....	46
Chapter 4	3D Printing and Applied Modifications for MRI RF Coil Printing	47
4.1	3D Printer Modification Process and Fabrication .....	47
4.1.1	Ink Printing Process .....	50
4.1.2	RF Coils for Print.....	52
4.1.3	Ink Resistivity Measurement .....	55

4.2	Fabrication Challenges .....	57
4.3	Summary .....	58
Chapter 5	Design of MTL Resonators and Measurement .....	59
5.1	MTL Resonator's Design Procedure .....	59
5.1.1	Permittivity and Loss Tangent Extraction .....	62
5.1.2	Substrate Design for Reduced Loss, Semi Air-filled Dielectric .....	64
5.2	Coil Simulation and Results .....	65
5.2.1	Matching Improvement .....	68
5.3	Printed MRI Coils Realization .....	69
5.4	Bench Measurement Setup and Return Loss Results .....	73
5.5	MR Measurement Results and Discussion .....	75
5.6	Summary .....	80
Chapter 6	Conclusion and Future Work .....	81
6.1	Summary and Conclusion .....	81
6.2	Future Study .....	82
6.3	MTL Resonators Fabrication Recommendations .....	83
References	.....	84
Appendix	.....	89

## List of Tables

Table 4-1: Thickness and sheet resistance values of measured lines.....	56
Table 4-2: The resistivity, sheet resistance for silver ink, and the resistivity of copper. The conductivity of copper is $5.96 \times 10^7 S/m$ . .....	56
Table 5-1: Complex permittivity for plastics used for RF coils .....	64
Table 5-2: The MTL resonator capacitor dimensions for PLA plastic .....	66
Table 5-3: The MTL resonator capacitor dimensions for ABS plastic.....	66
Table 5-4: The MTL resonator capacitor dimensions for UV-resin plastic.....	67
Table 5-5: The resonators type and built capacitors types.....	70
Table 5-6: Measurement values for Q factor, Loading factor ( $\eta$ ), and SNR for six coils. ....	75
Table 5-7: Calculated SNR values for Sagittal and coronal slices .....	79
Table A-1: Ink-process parameter settings .....	93

## List of Figures

Figure 2-1: Spin echo sequence .....	17
Figure 3-1: A surface loop coil with tuning and matching capacitors [12]. .....	20
Figure 3-2: The 8-channel head coil and a single element shown composed of a TEM resonator connected to automated matching circuit [30], IEEE copyright line @ June 2013 IEEE. ....	26
Figure 3-3: Microstrip resonator with matching and tuning capacitors at both ends [30], IEEE copyright line @ June 2013 IEEE .....	26
Figure 3-4: “Simulated $B_1$ field distribution in the transverse direction for the unloaded volume coil. $B_1$ field magnitudes at the center of all coils are normalized to 100%. The birdcage coil has better unloaded $B_1$ field homogeneity than TEM and microstrip coils [36]. .....	31
Figure 3-5: The circuit model with RF tuned to sample; a) RF coil inside the sample, b) RF coil separated from sample [32]. .....	32
Figure 3-6: measurement set-up as method to measure Q factor. Probes are placed at both sides orthogonal to $B_1$ field [24]. The above setup is for the unloaded case. ....	36
Figure 3-7: Desktop 3D printer at M2M laboratory- The University of Alberta..	44
Figure 3-8: Commercial FDM 3000 system [51]. .....	44
Figure 4-1: 3D desktop printer (X-series, Machina Corp, located at the University of Alberta, Electrical and Computer Engineering Department) is retrofitted with Regulator, Syringe, and a Dispenser (Ultimus V, Nordson) to print lines of conductive ink on the substrate. ....	49
Figure 4-2: Objet Eden350V (Stratasys) that prints UV-curable resin. It is located at Mechanical Engineering department, University of Alberta. ....	49
Figure 4-3: G-code example for substrate printing .....	51
Figure 4-4: Schematic view of a full MTL resonator .....	52
Figure 4-5: Resonator printed in sections of three, prepared for ink process. ....	53
Figure 4-6: G-code modifications for ink printing, no extrusion required. Syringe and extruder are raised above the surface. ....	54

Figure 4-7: 3D printing ink on resonator parts, (a) ink printed on PLA resonator with capacitors on both ends, (b) ink printing on ABS material as ground plane.	55
Figure 4-8: Four point probe used to measure the sheet resistance .....	55
Figure 5-1: CAD drawing of the 3D printed partially air-filled microstrip coil with integrated capacitors .....	60
Figure 5-2: MTL resonator showing conductive layers (red) and substrate (green) .....	60
Figure 5-3: Circuit model of resonator with tuning and matching capacitors .....	61
Figure 5-4: substrate-free areas are introduced into design to reduce the dielectric loading effects on MTL resonator performance. ....	65
Figure 5-5: Final capacitor dimensions for MTL resonator.....	66
Figure 5-6: The S11 (dB) simulated results showing match at 200MHz for three resonators .....	67
Figure 5-7: Smith chart model, resonance frequency matching at 200MHz for UV-resin resonator .....	68
Figure 5-8: Smith chart model, resonance frequency matching after iterations at 200MHz for UV-resin resonator. ....	69
Figure 5-9: Fabricated resonators with copper: (1,3) PLA and ABS with commercial tuning capacitors, respectively. (2) Standard resonator with low loss Rohacell foam, (4,5,6) ABS, Resin, PLA resonators with built-in parallel plate 3D printed capacitors. ....	71
Figure 5-10: (7) ABS with ink, (8) PLA with ink.....	71
Figure 5-11: S11(dB) loaded-matching in simulation results showing two 3D-printed ABS and PLA resonators with silver ink as conductive layer.....	72
Figure 5-12: loaded matching bench measurement set-up, matching resonators to 200.4MHz for 4.7T MRI system.....	74
Figure 5-13: Matching S11 (dB) loaded measurement results. ....	74
Figure 5-14: Sagittal slice 1 and the SNR for six different coils are shown.....	76
Figure 5-15: Sagittal slice 2 and the SNR for six different coils are shown.....	77
Figure 5-16: Sagittal slice 3 and the SNR for six different coils are shown.....	77

Figure 5-17: Coronal image of six resonators with SNR bar. Numbers correspond to type of resonators in Table 5-7. This image is driven from 8×15cm of the field of view. ....	78
Figure 5-18: Sagittal image of six resonators with their SNR bar. Numbers correspond to the type of resonators as shown in Table 5-7.....	79
Figure A-1: Different tabs of Slic3r program 1: the plater, 2: the print settings. .	90
Figure A-2: Different tabs of Slic3r program 1: the filament setting, 2: the printer settings. ....	91
Figure A-3: The resonator shown flipped (left) and in the printing orientation (right). The skirt is printed around in both cases so the resonator can be positioned accurately for ink or additional layer printing. ....	93

## **List of Abbreviations**

Magnetic Resonance Imaging (MRI)

Radio-Frequency (RF)

Nuclear Magnetic Resonance (NMR)

Computed Tomography (CT)

Microstrip Transmission Line (MTL)

Additive Manufacturing (AM)

Computer Aided Design (CAD)

Acrylonitrile Butadiene Styrene (ABS)

Poly Lactic Acid (PLA)

Signal to Noise Ratio (SNR)

# Chapter 1 Introduction

## 1.1 Background

Magnetic Resonance (MR) is one of the most important medical imaging methods. MR imaging is the process of generating high contrast images without the ionizing radiation that is used in other methods such as computer tomography (CT). In the 1970's, MRI technique was used to generate tomographic images from a thin slice of human body. After decades, thanks to the work of many researchers, MRI has advanced and has become a volume imaging technique. Also, Spectroscopy and MRI techniques in combination are used to generate very informative diagnostic images.

RF coils are essential in MR imaging, as they are used to transmit RF signal to body and receive the MR signal back from it. In general, RF coils are designed to be used to transmit, receive or both. Typically, RF coils are made with low loss dielectric substrates such as low loss foams and copper tapes. For any MR scanner, a Larmor frequency is defined based on its static magnetic field. In order to transmit RF signals to the body and receive the signal efficiently, RF coils need to be matched to  $50 \Omega$  since they are connected to the RF amplifiers through coaxial cables. Also, the coils must be tuned to Larmor frequency of the static magnetic field. In a standard RF coil, matching/tuning capacitors are used for these purposes.

MTL (microstrip line resonator) is composed of a signal line laid on low loss material such as dielectric. Matching/tuning capacitors are usually soldered to MTL resonator, but finding the required capacitors and the repetitive soldering task can be an issue during fabrication.

3D printing, an emerging technology that replaces the traditional fabrication methods, has been introduced as an additive manufacturing technique that builds a 3D prototype from a 3D model. 3D printers vary in cost based on their printing resolution, printing process, and materials used in the printing process. A typical

low cost desktop printer's price is around \$2500 CAD. A desktop 3D printer has one extruder to lay down the plastic material on the print bed.

In this thesis, a low cost 3D printer is modified and used to design microstrip transmission line coils for MRI systems. It will be shown that such systems can be used to generate high quality MR compatible coils.

## **1.2 Motivation and Objective**

Additive manufacturing is a direct path from a 3D model to a prototype or final product, and it involves less processing steps compared to conventional fabrication methods. 3D printing is introduced as a new approach to build MRI coils— a custom 3D model is imported to a low cost desktop 3D printer and within few hours, a coil is fabricated. 3D printing of MRI coils provides the flexibility of manufacturing cost-effective and custom designed RF coils for MR applications. Standard MR microstrip coils use low loss foams as substrate and MR compatible, high Q factor, commercial, variable/fixed capacitors for matching/tuning purpose. Typically, in coil design, matching/tuning capacitors need to be soldered for connections. In case of different loadings (patients), repetitive labour-intensive work of soldering becomes inevitable. Availability, high cost, soldering issues of matching/tuning capacitors encourage adopting 3D printing to build MR coils.

The fabrication process with 3D printing reveals new possibilities for MR compatible coils and demonstrates its benefits in design and fabrication. 3D printing technology offers the possibility of having the state of the art 3D-printed parallel plate capacitors monolithically integrated with 3D-printed coils. In addition, the coil can be fine-tuned for any load at the design stage, which eventually results in higher quality structures. Taking advantage of 3D printing technology, the issues such as cost and soldering are eliminated. One of the main advantages of 3D printing technology in MRI coil design is that the 3D structural model can be altered to minimize the amount of substrate that is used in design, which consequently, lowers the total effective loss tangent and increases the coil's efficiency and signal to noise ratio (SNR).

There is no low cost 3D printer that allows building a prototype with metal and plastic material in one machine. Here, a low cost 3D printer is customized to

add the possibility of conductive ink printing. To implement the idea, a bench-top, low cost 3D printer has been utilized and accordingly modified. The enhancements on the existing machine are also explained in this thesis. The aim here is to design, 3D print, and characterize the MR compatible coils for 4.7T system. The MRI coil design and characterization to adapt to 3D printing technology is explained next.

In this thesis, thermoplastic materials will be used to fabricate MTL resonators for 4.7T MRI system. Since these materials' RF performance is not known, a characterization process has to be developed to investigate their permittivity and loss tangent at 200 MHz - the Larmor frequency of the 4.7T scanner. A low cost 3D printer (Xseries, Machina Corp) will be retrofitted to add the capability of ink-printing to it. Then, MTL resonators with built-in parallel plate matching/tuning capacitors will be designed and 3D-printed. Various MTL resonators will be fabricated with copper tape or silver ink, and their performance in terms of quality factor and signal to noise ratio (SNR) will be compared to a standard low loss foam resonator.

In this thesis, for the first time, the state of the art design and 3D printing procedures of parallel plate matching/tuning capacitors for MTL coils will be described. Also, for the first time, a low cost 3D printer is customized to add ink printing capability.

### **1.3 Thesis Structure**

This thesis is composed of five chapters. A brief introduction of MR imaging and motivation of thesis are outlined in Chapter 1. A comprehensive literature review, including basic MRI concepts and different imaging techniques, is provided in Chapter 2. Various RF coils used in MRI with their performance evaluation processes and 3D printing technologies are described in Chapter 3.

In Chapter 4, the modification process to add capability of ink-printing for a low cost desktop 3D printer is addressed. In Chapter 5, the design procedure of MTL resonators and their simulation and measurement results are shown. Finally, Chapter 6 concludes the research and outlines the findings within this thesis.



## Chapter 2 MRI Theory

Magnetic resonance imaging (MRI) is a process of generating high contrast images of the body without the ionizing radiation that is used in other modalities such as X-rays and Computed Tomography (CT).

The first MR prototype equipment was developed by Jim Hutchison, Bill Edelstein and their colleagues in 1974 and was used to take images from a rat [1]. MRI imaging was initially based on proton weighting. T1 weighted images were introduced for clinical applications. Later in 1982-1983, T2-weighted spin echo images proved to provide better contrast and replaced older imaging techniques for clinical MRI imaging [1].

A big superconductive magnet is used to produce high magnetic field necessary to acquire images. The nuclei has a proton and neutron that are bonded together with nuclear forces. Spin is a fundamental property that is in multiples of  $1/2$  and can be positive or negative. The spin for a single proton is like magnetic moment vector, and the proton possess two magnetic poles, + and -. When these protons are placed inside the magnetic field of MRI, the spin vector of proton is aligned with the magnetic field. In order to be NMR (Nuclear Magnetic Resonance) viable, the nuclei must have nuclear magnetic moment. The nucleons (protons and neutrons) have magnetic moments from circulating currents that are internal to nucleus. If the number of either nucleon type is odd, such as odd-even, and odd-odd nuclei, the nuclei is NMR viable. The resonance frequency of the protons has direct relation with the strength of MR magnet. For imagining, an element must have a fractional spin ( $1/2$ ,  $3/2$ , and  $5/2$ ) [1]. Luckily, human tissue is composed of 63% of H (Hydrogen) which has the spin of  $1/2$  [1]. By taking advantage of this fact, standard MRI uses hydrogen for imaging.

As it was described before, in the human body, protons have their own magnetic moment vector, and when these atoms are placed in a large external magnetic field (of main magnet) they are divided into lower and higher energy states. In order to move from a low to high energy state, absorption of photon is

required. The energy of this photon is equal to energy difference between the two states.

The quantity of low energy level atoms is higher than high energy atoms. The net magnetization  $M_0$  is a vector generated from population difference between two energy state's magnetic moment vectors, as of all small magnetic field vectors of protons that aligned to main magnetic field and the ones aligned in opposite direction. In the reference [2], the description of magnetization of nuclei in the body is provided. The magnetic moment is given by:

$$\mu = \gamma \hbar \mathbf{I} \quad (2-1)$$

in equation (2-1),  $\mu$  is the magnetic moment of protons,  $\gamma$  is the gyromagnetic ratio and  $\hbar \mathbf{I}$  is the spin angular momentum. The energy of magnetic moment inside main magnet's static field  $B_0$  is:

$$E = -\mu_z \cdot B_0 \quad (2-2)$$

in the equation above, E is the energy of the spin state, and  $B_0$  is the static magnetic field which is considered along Z-axis in this thesis. When body is placed inside the static magnetic field, low energy spins that are shown as  $I=1/2$ , are aligned with direction of static magnetic field, and high energy spins are antiparallel to direction, that are shown as  $I=-1/2$  energy state. If we consider the number of protons in parallel with the main magnetic field as  $n^\uparrow$ , and the number of antiparallel spins as  $n^\downarrow$ , the difference in the energy states can be shown as:

$$\frac{n^\uparrow}{n^\downarrow} = e^{\frac{\gamma \hbar B_0}{k_b T}} = e^{\frac{\Delta E}{k_b T}} \quad (2-3)$$

The energy difference between low energy (parallel) and high energy states (antiparallel) equals to a photon with energy shown in equation (2-4), which is related to the Larmor frequency of static magnetic field, and it can be shown as:

$$\hbar \omega_0 = \gamma \hbar B_0 \quad (2-4)$$

where  $\omega_0$  is the Larmor frequency. The presence of the static magnetic field will generate a torque on protons that can be shown as [2]:

$$\frac{\partial(\mathbf{I}\hbar)}{\partial t} = \frac{1}{\gamma} \frac{\partial(\boldsymbol{\mu})}{\partial t} = \boldsymbol{\mu} \times (B_0 \hat{\mathbf{z}}) \quad (2-5)$$

$B_0$  is the static magnetic field in Z axis direction which will cause a torque in protons and ultimately the change in the magnetic moment of protons can be shown as:

$$\frac{\partial(\boldsymbol{\mu})}{\partial t} = \gamma B_0(\mu_y \hat{x} - \mu_x \hat{y}) = \omega_0(\mu_y \hat{x} - \mu_x \hat{y}) \quad (2-6)$$

and,

$$M_0 = \frac{(B_0(\gamma\hbar)^2)N}{4kT} \quad (2-7)$$

in equation (2-7), the nuclear magnetization is shown with direct relation to static magnetic field and number of spins N per unit volume. The precession can be defined as the effect of static magnetic field  $B_0$  on the magnetic moment of nuclei  $\mu$ , and that can be modeled as [3]:

$$\frac{d\boldsymbol{\mu}}{dt} = -\gamma B_0 \wedge \boldsymbol{\mu} \quad (2-8)$$

The resulting forces from the magnetic moment on  $\hat{\mu}$  is negligible [3], and vector  $\hat{\mu}$  starts rotating around the axis of  $B_0$  with frequency in equation (2-9). The magnetic resonance frequency is defined based on the frequency of rotation of protons around the axis of the main magnetic field. The resonant frequency has direct relation with static magnetic field.

$$\boldsymbol{\omega}_0 = \gamma \mathbf{B}_0 \quad (2-9)$$

The gyromagnetic ratio for hydrogen atom is 42.57MHz/T [1]. Equation (2-6), in order to represent total magnetization, has to include the lattice and longitudinal relaxation. In fact, the Bloch equation represents that effect [2]:

$$\frac{\partial(\mathbf{M})}{\partial t} = \gamma \mathbf{M} \times \mathbf{B} - \frac{\mathbf{M}_{xy}}{T_2} - \frac{M_z(t) - M_z(0)}{T_1} \hat{z} \quad (2-10)$$

in equation (2-10),  $M_z$  and  $M_{xy}$  are the longitudinal and transverse magnetizations, respectively.

In order to measure MR signal we require a dynamic magnetic field. This is done by RF coils which generate a perpendicular magnetic field to the direction of main magnetic field. When a body is placed in the main magnetic field, group of spins take one orientation (parallel or antiparallel to the direction of static magnetic

field). The population difference between parallel and antiparallel states defines the net magnetization.

The RF-pulse is produced using RF coils to rotate the spins from longitudinal plane to the transverse plane. Basically the magnetization  $M_0$  is tilted to the transverse plane. The important point is that since the protons with net magnetization rotate with frequency of  $\omega_0$ , the force (RF pulse) must have the same frequency. If we assume that the net magnetization is located in xy plane, after applying RF pulse, the net magnetization will rotate around the  $\hat{z}$  axis with frequency equal to the frequency of photons that can make an upward or downward transitions from the energy states. By matching the frequency of RF pulse to the Larmor frequency, the rotating axis for atoms from longitudinal axis  $\hat{z}$  can be tilted to transverse plane xy, with a relatively small magnetic field compared to the static magnetic field [1]. Three main conditions are important to be considered here for RF-pulse application:

- RF coil must have the same frequency with the protons in the magnetic field
- RF pulse duration must be long enough to be able to achieve the required flip angle for protons from z to xy plane
- RF pulse (dynamic magnetic field  $B_1$ ) should be perpendicular to static magnetic field's plane

If these conditions are met, then the RF-pulse will be more efficient. The MR signal can be picked up from the net magnetization by having a receive coil. The net magnetization on transverse axis can produce a current in the receiving coil according to the Faraday's Law [1]. In order to show the precession, the rotating reference frames are defined as:

$$\begin{aligned}
 \mathbf{x}' &= \cos(\omega t) \hat{\mathbf{x}} - \sin(\omega t) \hat{\mathbf{y}} \\
 \mathbf{y}' &= \sin(\omega t) \hat{\mathbf{x}} + \cos(\omega t) \hat{\mathbf{y}} \\
 \mathbf{z}' &= \hat{\mathbf{z}}
 \end{aligned}
 \tag{2-11}$$

now, by incorporating the equations (2-10) and (2-11) we have:

$$\frac{\partial(\mathbf{M}_{rot})}{\partial t} = \gamma \mathbf{M}_{rot} \times (\mathbf{B}_0 + \frac{\omega}{\gamma} + \mathbf{B}_1) - \frac{\mathbf{M}_{xy}}{T_2} - \frac{M_z(t) - M_z(0)}{T_1} \hat{\mathbf{z}} \quad (2-12)$$

in which  $M_{rot}$  is the rotating magnetization,  $B_0$  is the static magnetic field, and  $B_1$  is the rotating magnetic field with precession  $\omega$ . If a homogenous rotating magnetic field  $\mathbf{B}_1$  is applied in the rotating frame along x axis with time, the magnetization after applying the RF pulse will be [4]:

$$\mathbf{M} \approx M_0(\cos(\alpha) \mathbf{z}' + \sin(\alpha) \mathbf{y}') \quad (2-13)$$

in which,

$$\alpha \approx \gamma \int B_1 dt = \tau \gamma B_1 \quad (2-14)$$

flip angle  $a$  defines the degree of excitation in which the net magnetization is rotated relative to  $B_0$  direction. The RF pulse at Larmor frequency defines the flip angle. The degree to which the net magnetization is rotated depends on strength of  $B_1$  and its duration  $\tau$ . In order to receive the signal back from sample (body), the coil should be matched to the same Larmor frequency of the static magnetic field. If a receive coil is placed above the body, an induced voltage is generated on the coil loop that can be shown as [2], [4]:

$$S(t) = e^{\frac{i\pi}{2}} \omega_0 \int_V \hat{B}_1^-(r) \mathbf{M}_{xy} e^{-i(2\pi k(t) \cdot r + \omega_0 t)} dr \quad (2-15)$$

in which,  $k(t)$  is the position in K space, and  $\hat{B}_1^-(r)$  is the left circularly polarized magnetic field that is produced by coil per unit current [4]. As it can be seen from equation (2-15), the received signal is directly proportional to the coil sensitivity,  $\hat{B}_1^-(r)$ , and the magnetization in the transverse plane.

$$\begin{aligned} B_1^+ &= B_1 \exp(-i\omega_0 t) \\ B_1^- &= B_1 \exp(i\omega_0 t) \end{aligned} \quad (2-16)$$

here,  $B_1^+$  is the clockwise circularly polarized component of the transmit magnetic field, and  $B_1^-$  is the counter clockwise circularly polarized component of the receive field which rotates in opposite direction to the magnetization [5], [6].

## 2.1 Relaxation

After excitation with RF pulse, the magnetization gradually recovers its longitudinal alignment that was originally aligned in the direction of the static magnetic field. This process is called longitudinal relaxation.

Initially, the magnetization is along the Z direction in fixed laboratory frame. Then, RF pulse  $B_1$  with time duration  $\tau$  is applied and altered the magnetization  $M_0$  to  $M_{xy}$ . Hereby, the RF pulse creates two components: a longitudinal component along Z axis, and a transverse component on xy plane. The longitudinal component is positive if the flip angle  $\theta < 90^\circ$ , and negative if  $\theta > 90^\circ$ . After RF pulse, the amplitude of longitudinal magnetization is increased and gains the thermodynamic equilibrium [3]:

$$\frac{dM_z(t)}{dt} = -\frac{M_z(t) - M_0}{T_1} \quad (2-17)$$

the transverse magnetization changes according to:

$$\frac{dM_{xy}(t)}{dt} = -\frac{M_{xy}(t)}{T_2} \quad (2-18)$$

$T_1$  and  $T_2$  are called spin-lattice relaxation and spin-spin relaxation, respectively. It has been found experimentally that  $T_1 \geq T_2$  [3]. Spin-lattice relaxation happens at the same time when spin-spin relaxation is started. The spin-spin relaxation continues until the point  $\overrightarrow{M_{xy}} = 0$ , where the net magnetization at transverse plane is zero. Also, the time duration for RF pulse is generally much smaller than relaxation time  $\tau \ll T_2 \leq T_1$ . Relaxation time is originated from entirely random magnetic fields inside the sample [3]. The magnetic flux variation resulting from relaxation components creates a signal in receive coil which is tuned at the precession frequency (Larmor frequency) [3].

As we discussed about transverse magnetization, after the  $90^\circ$  RF pulse, the spins start dephasing from each other, and that leads to decay of transverse magnetization. In fact the transverse decay can be modeled as exponential decay:

$$\mathbf{M}_{xy}(t) = \mathbf{M}_{xy}(0)(\exp(-t/T_2)) \quad (2-19)$$

The dephasing can also be caused by inhomogeneity in the main magnet.  $T_2^*$  accounts for the static magnetic field inhomogeneity and magnetic susceptibility.

$$\frac{1}{T_2^*} = \frac{1}{T_2} + \frac{1}{T_2'} \quad (2-20)$$

in which  $T_2'$  stands for the static inhomogeneity. Therefore signal decay is faster with  $T_2^*$ , since more dephasing is present. The relaxation times are function of the static magnetic field.

## 2.2 Signal Detection

$M_{xy}$  rotates in the xy plane with frequency of  $\omega_0$ , if a RF receive coil is placed in the way that  $B_1$  is orthogonal to  $B_0$ , a current is generated on the coil based on Faraday's principle and we can detect the signal. This current is called MR signal [1]. The electromotive force  $e$  is shown as [3]:

$$e = \int \vec{E} \cdot d\vec{l} \quad (2-21)$$

where,

$$\vec{E} = - \frac{\partial \vec{A}}{\partial t} \quad (2-22)$$

in equation (2-22),  $\vec{A}$  is the magnetic vector potential created from variation by time in the transverse magnetization [3]. If we assume a sample  $\delta V$  within a volume of  $V$ , the transverse magnetization will be  $\vec{m}_{xy}(t) \delta V$ . And the electromotive force that can be detected with a receive coil only from that sample in the volume is shown as [3]:

$$\delta e = - \frac{\partial}{\partial t} \left[ \frac{\vec{B}_1}{l} \vec{m}_{xy}(t) \right] \delta V \quad (2-23)$$

in which the division of  $\frac{\vec{B}_1}{l}$  is the field per unit current at position  $\delta V$ . As it was described earlier in Chapter 2,  $B_1$  is composed of equation (2-24) and the longitudinal part  $B_{1z}$  [7]:

$$\begin{aligned}\overrightarrow{B^+}_1 &= \frac{B_{1x} + iB_{1y}}{2} \\ \overrightarrow{B^-}_1 &= \frac{(B_{1x} - iB_{1y})^*}{2}\end{aligned}\tag{2-24}$$

$\overrightarrow{B^+}_1$  is the clockwise circular polarized magnetic field, and  $\overrightarrow{B^-}_1$  the counter clockwise polarized magnetic field. Here, it must be stressed that coil's frequency bandwidth must contain the precession frequency of the static magnetic field. The reciprocity theorem states that the received MR signal from sample is proportional to intensity of magnetic field ( $B_1$ ), which is the magnetic field at the location at receive coil [8]. In fact, receive coil detects the electromotive force  $e$  from magnetic field in the area of sample.

The signal that is detected from a sample comes from the amount of magnetization in the region of interest. To this end, in the next section, the effect of spatially varying magnetic fields on received signal from transverse magnetization is reviewed.

### 2.3 Spatial Encoding and Gradients

Basically, when a patient (sample) is outside the scanner, the protons inside his/her body have magnetic moment, but as we place a patient inside MRI scanner, the magnetic moment vector of spins align with the main magnetic field's direction. Now, if we place a receive coil, the detected signal will include information about protons all over the body. The echo time, when we acquire the image, fits into the time interval between the time where  $M_{xy}$  is at highest level (the transverse magnetization is maximum) until it decays by time. Basically, the image is a 2D slice that contains pixels as such that each pixel has a thickness information related to it and that is the basic of spatial information of imaging. In fact, the size of voxels and the number of phase and frequency encoding steps will determine the size of spatial space. The main concept here is to manipulate the total magnetization of the region of sample using gradients and encode their spatial information inside the volume. Spatial encoding means labeling protons with small frequency change with respect to their location in the volume, and then giving each proton a frequency

slightly more or less than its precession frequency. If we look at their MR signal frequency component, the spatial coordinates of protons can be located [1]. This is called spatial encoding and changing the spatial frequency is done by phase-encode gradients.

In general steps, first, the slice is selected using slice selection gradient which is ON during the rotating RF pulse, then with a sequence of phase and frequency encoding gradients, the localization is addressed inside the selected slice. Gradients in MR has 1-3% of the strength of main static field, and essentially two gradients is necessary to encode the magnetization signal spatially [1]. Gradients coils are essential to produce linear DC magnetic fields for spatial encoding. This is done so that the magnetic field can be stronger in some directions than others. These coils carry current and produce magnetic fields in three directions x, y, and z. Three gradient coils, in which their linear magnetic field can vary based on the current going through them, are placed inside the magnet, and it has to be stated that their magnetic fields are superimposed on the main magnetic field,  $B_0$ . By varying their gradient fields, each signal locates a spatial point in the volume. In spatial encoding, the easiest one is the slice selection, followed by a frequency and phase encoding. The K-space is a 2D space that the MR image is acquired from. K-space is made from received signal data. The MR image can be made by Discrete Fourier Transform from K-space.

Two magnetic coils that are electrically joint are placed on the scanner, DC current goes in opposite direction into them and produces the Z gradient. Since they have opposite magnetic fields, the gradient will be zero at the iso-centre of the scanner. If a homogenous static magnetic field  $B_0$  is present, and RF pulse of  $\tau$ , and  $B_1$  is applied, the signal at iso-center only has the transverse magnetization information, but not gradient. This means that the protons at iso-center spin only at Larmor frequency. If we consider moving along Z direction from iso-center, the signal will include gradient information as well. Therefore, the transverse magnetization only happens at iso-center of MR, and the rest doesn't have useful information. Since the gradient is linear and we know the strength of it, we can

predict the precession frequency at each location along Z direction. Simply by adjusting the transmit RF frequency, we can select the locations that we require.

As there are three built-in orthogonal gradients in MR scanner, if we want a coronal image, we turn ON the y gradient and slices are selected perpendicular to the plane of gradient. If an RF pulse is applied at the same time with slice select gradient, and the bandwidth of RF pulse is  $\Delta f$ , the selected slice thickness will be [3]:

$$\Delta u = \frac{2\pi\Delta f}{\gamma G} \quad (2-25)$$

Therefore, the bandwidth of RF pulse determines the thickness. In order to generate an oblique slice we have to use more than one gradient at each time. In order to change the orientation, multiple gradients can be applied as vectors and the vector sum of those components represents the orientation of net magnetic field. RF coils send a Sinc pulse that is an envelope of signal with small bandwidth. In fact we can't just transmit the Larmor frequency. Now, in order to select a slice, a DC current should be applied, and the highest current is used to obtain higher resolution.

The slice selection gradient should be ON at the same time of RF pulse transmitted, and when the slice is selected, both RF and gradient are OFF. At the acquisition time a gradient must be ON in order to have amplitude and frequency information within the slice. If a gradient is ON and we are sampling the signal, each point in the selected slice will have different frequency and amplitude because of the linear nature of gradient and the type of tissue. All these information is embedded into the signal that we receive with coil, but it has to be done while the signal is being sampled (frequency encoding). The sampled signal has information about frequencies and amplitude of the selected slice. In order to process that data, an analog to digital converter gets the sampled complex signal from the receive coil and samples it. An image can be created using Fourier transformation of the K-space data, and MR image is generated based on the magnetization differences within the tissue slice.

The gradient has to be perpendicular to the slice selection gradient. At this stage the frequency within the slice can be modeled as:

$$\omega = \gamma(B_0 + G \cdot r) \quad (2-26)$$

In order to find information about phase, a phase encoding gradient must be applied between the time interval when RF and slice selection gradient are OFF, and acquisition. At that time interval and before phase encode gradient, the spins are rotating at the same frequency. When a phase gradient is applied, the spins get different phase shifts, and when the gradient is OFF, they spin at the same frequency with different phase. Hence at the time of sampling they will have a phase shift according to the phase encode gradient strength.

The phase gradient also has iso-center. And when moving towards the iso center, the difference in phase encoding magnitude between the gradient and iso center becomes lesser. Therefore, the final image is generated with frequency information, and phase difference information. Discrete Fourier Transform (DFT) is essential to achieve this information. The DFT is used to detect the relative changes in signal amplitude and phase differences arising from the gradient fields within the slice.

TR and TE are pulse sequence parameters. TR is the repetition time and TE is the echo time. Every line of image for phase encoding happens in one TR, hence the total imaging time will be shown as:

$$T_{image} = TR \cdot N_p \quad (2-27)$$

in which,  $N_p$  stands for number the phase encoding steps. A point in K-space, which is a space in time domain is defined as:

$$\mathbf{k}(t) = \frac{\gamma}{2\pi} \int \mathbf{G}_r dt \quad (2-28)$$

in the equation (2-28),  $G_r$  is the vector of gradient applied, and t is the time which gradient was applied. The gradients are applied to encode the signal and phase information on the k-space and the DFT is applied to produce an image. In order to model the 3D image, the density of magnetization inside the volume is

$\rho(x, y, z)$ , where three orthogonal gradients  $G_x, G_y, G_z$  are applied within time durations of  $\tau_x, \tau_y, \tau_z$  and the Fourier transform will be modeled as [3]:

$$\mathbf{S}(x, y, z) = \int_x dx \int_y dy \int_z dz \cdot \rho(x, y, z) \cdot e^{-j2\pi(K_x x + K_y y + K_z z)} \quad (2-29)$$

in equation (2-29), the reciprocal values are measured in 1/m:

$$\begin{aligned} K_x &= \frac{\gamma G_x \tau_x}{2\pi} \\ K_y &= \frac{\gamma G_y \tau_y}{2\pi} \\ K_z &= \frac{\gamma G_z \tau_z}{2\pi} \end{aligned} \quad (2-30)$$

and the phase information can be written as follow:  $\vec{K} \cdot \vec{r} = K_x \cdot x + K_y \cdot y + K_z \cdot z$ .

## 2.4 Image Contrast

The spin-lattice relaxation  $T_1$  is relatively long compared to spin-spin relaxation  $T_2$ . Spins with their interaction to each other facilitate the  $T_2$  relaxation time. It means that the liquids with less interaction between spins will have longer transverse magnetization decay as opposed to volumes with high spin-spin interaction. On the other hand the difference between tissues in terms of  $T_1$  is related to spin-lattice interaction.

But in order to calculate  $T_1$ , multiple excitations are required to determine  $M_0$  and  $M_z$ , and then  $T_1$  is extracted. By choosing echo time (TE), a  $T_2$  contrast image can be made. The decay of transverse magnetization  $M_{xy}$  after a RF pulse is an exponential decay which is different for different tissues. The signal can be detected with a RF receive coil and is called free induction decay (FID). In equation (2-31), the longitudinal magnetization after  $90^\circ$  pulse is shown:

$$\mathbf{M}_z(t) = \mathbf{M}_0(1 - \exp(-t/T_1)) \quad (2-31)$$

### 2.4.1 Inversion Recovery Sequence

This sequence is used to represent the longitudinal relaxation after  $180^\circ$  RF pulse. If two tissues with different proton densities are placed in the scanner, then

one  $180^\circ$  RF pulse with duration of  $\tau$  is applied to make the net magnetization along  $-Z$  axis, which is represented as  $-M_z$ . After this pulse, spins start longitudinal relaxation to return to their relaxation point along  $+Z$ , and they will cross the point of zero longitudinal magnetization. The time that it takes their relaxation to reach zero depends on  $T_1$ . A tissue having longer  $T_1$ , will have its relaxation reaching zero slower than one with shorter  $T_1$ . This sequence is called Inversion Recovery. In equation (2-32), the longitudinal magnetization recovery is shown after an inversion RF pulse of  $180^\circ$ :

$$M_z(t) = M_0(1 - 2\exp(-t/T_1)) \quad (2-32)$$

### 2.4.2 Spin Echo Sequence

The spin echo pulse sequence is commonly used in MR imaging. It is refocusing the spin magnetization using a series of RF pulses. This sequence is created with event of  $90^\circ$  and  $180^\circ$  re-phasing pulses at  $TE/2$ . The repetition time is TR; at each TR a vector of points in K-space will be generated, which is done by using frequency and phase encoding gradients as explained in the previous sections. The  $180^\circ$  pulse is used here to re-phase the spins that are dephasing mainly due to the static field inhomogeneity and spin-spin relaxation. Therefore, an image after  $180^\circ$  is  $T_2$  weighted, since the inhomogeneity effect is being compensated by this RF pulse.

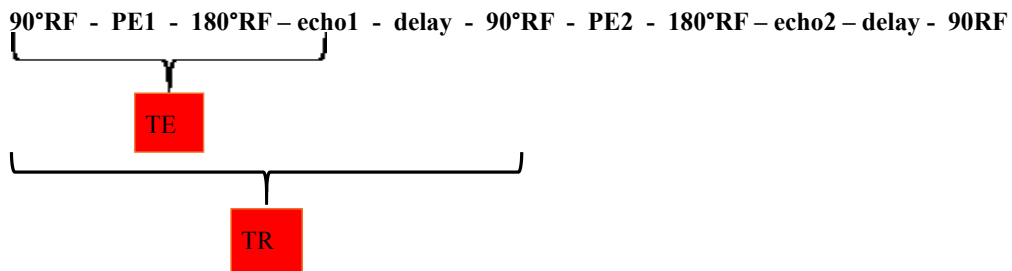


Figure 2-1: Spin echo sequence

The duration of spin echo can be defined as:

$$\text{Duration SE} = \text{TR} \cdot N_p \cdot N_{ex} \quad (2-33)$$

in equation (2-33),  $N_p$ , and  $N_{ex}$  represent the number of phase encoding and number of excitation, respectively. For each phase encode step an echo is taken and

this cycle is repeated for each TR. Spin echo has two important parameters, TR and TE, which can determine the contrast of the image. TR is the time between two excitation RF pulses. The TR that is repeated after every  $90^\circ$  pulse is chosen to provide contrast based on the tissue's spin-lattice relaxation time  $T_1$ . If the TR is long, then the tissue has a long longitudinal magnetization recovery. TE is the time elapsed between excitation RF pulse and echo. Basically in a  $T_2$ -weighted image, TE and TR are chosen to demonstrate the  $T_2$  relaxation. If an image is taken with short TE and long TR, the contrast will be from proton density since high amount of transverse magnetization is yet to decay. Therefore, a long TR and a short TE will suppress the effects of relaxation times.

### **2.4.3 Gradient Echo**

This sequence is different from spin echo sequence in terms of the RF pulse that can produce a flip angle between  $0^\circ$  to  $90^\circ$ . In gradient echo sequence, the spin flip angle usually takes a smaller degree as opposed to spin echo and therefore the amount of transverse magnetization which will be detected with a coil in the scanner depends on TE and TR times. As a result of smaller flip angle, the longitudinal recovery time is smaller. In gradient echo, the acquisition time for image is small, hence the scan time is shortened.

Also, there is no  $180^\circ$  RF pulse in this sequence which reveals the fact that there is no compensation for inhomogeneity of static magnetic field and magnetic susceptibility, therefore the detected signal is  $T_2^*$ -weighted [9].

## Chapter 3 Literature Review

This thesis focuses on developing RF coils based on 3D manufacturing, which requires a solid knowledge of both RF coil theory and 3D manufacturing techniques. Since this is the first time such study has been conducted, we will review each of these categories separately. Section 3.1 will focus on RF coils and section 3.2 will emphasize additive manufacturing and 3D printing.

### 3.1 RF Coils

RF coils can be represented as an “antenna” for MRI scanners. An electric current in a loop of copper generates a magnetic field [8]. RF coils in MRI are made to transmit the RF energy and receive the signal back from the patient’s body. The application of RF coils in MRI will be better understood if some applications and challenges are addressed as below:

- RF coils are used to transmit and/or receive
- Signal to noise ratio (SNR) is limited by small detected signal from tissue and noise from sample
- Need to increase coupling between RF coil and sample

The RF coils are categorized into surface coils and volume coils. Solenoid coils are one type of volume coils that are used in NMR [8]. Surface coils can be used as receiver only, and another coil (a volume coil) is used as transmit coil only. Also, RF coil can transmit and receive as well; such a coil is called a transceiver coil. Surface coils are typically made of circular wire or copper tape loop in connection with capacitors to make resonant circuit [10]. The surface coil will be placed on the small region of the body, and it will pick up the signal from that region with high signal to noise ratio (SNR). Surface coils were introduced mainly to detect signal from samples that are larger than a solenoid coil and/or for localized signal detection from samples [8]. It has to be stated that the received magnetic field ( $B_1^-$ ) strength efficiency drops rapidly when moving away from coil; these coils are typically inhomogeneous. The radius of surface coil can be chosen to be equal to the thickness of region of sensitivity [8] in order to balance the inhomogeneity and

sensitivity. Using two single loop coils in a scanner as one single loop coil placed in  $\hat{x}$  axis, orthogonal to static magnetic field axis  $\vec{z}$  that its magnetic field be  $B_1\hat{y}$ , and other one placed in  $\hat{y}$  axis as its magnetic field has  $90^\circ$  phase difference  $jB_1\hat{x}$ , the circular polarized magnetization will increase the transmit efficiency by saving a factor of 2 in transmitted power and received signal to noise ratio (SNR) by  $\sqrt{2}$  [11], [8].

RF coil are used in single element form or in the form of array to transmit or receive signal in MR. The performance of RF coil is characterized based on their quality factor (Q), and signal to noise ratio (SNR) values. RF coils in array configuration provide higher SNR and better  $B_1$  homogeneity compared to one single element. Typically, RF loop coil is composed of a loop of copper conductor and tuning/matching capacitors soldered on the loop in order to match the coil to  $50\Omega$ , which is the input impedance of preamplifier (in the case of surface coil) and the input impedance of RF amplifier if the loop is used in transmit. A surface coil loop is shown in Figure 3-1 [12].

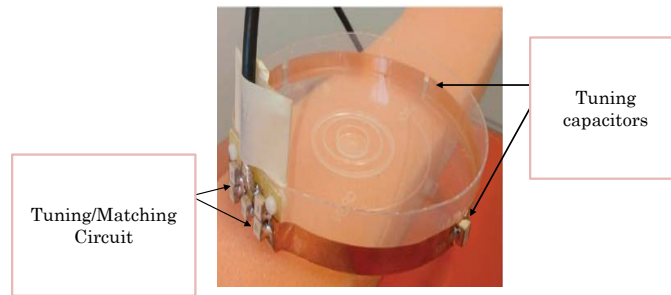


Figure 3-1: A surface loop coil with tuning and matching capacitors [12].

Tuning and matching capacitors are usually soldered on the coil, and this can be a labour-intensive work when using the coil for different samples, since dielectric and inductive coupling between coil and sample varies. Variable trimmer capacitors also have been used to adjust the coils with different samples, but they are costly.

Since matching and tuning capacitors are critical part of RF coil, in this thesis, a state of the art design of parallel plate capacitors integrated with MTL resonator is represented to MR applications.

It has to be stated that the cost of MR compatible high Q capacitors can be considerably high in higher magnetic fields. Therefore, a new technology that leads us in the direction to build RF coils with lower cost and lesser fabrication iterations is favourable.

### 3.1.1 Transmit Arrays

RF transmit array coils are designed to improve transmit  $B_1$  uniformity, SNR and to reduce the RF power required for transmit. Parallel excitation sources are required for transmit arrays. There are some limiting factors in design of transmit arrays: coupling between coil elements, dynamic range of  $B_1$  over sample, and coil geometry. The selective parallel excitation is typically done on a transmit volume coil that is driven in quadrature [13], [14]. In receive arrays, decoupling between elements is done using low-impedance preamplifiers that reduce the current flowing in each coil element [15]. One method that can reduce the coupling between transmit elements compared to loop coils is to use microstrip transmit elements in the array configuration [16].

The RF field  $B_1$  created by transmit coil needs to be homogenous in order to have the same flip angle at the desired volume for imaging. In higher magnetic fields, the inhomogeneity of RF magnetic field due to wave propagation increases and it is difficult to create a homogenous RF field inside the sample [17]. A partly homogenous field can be created using distributed currents in the elements of transmit array, where the current distribution is frequency and sample dependent [18]. RF shimming is done in order to maximize the signal received from the body. In a transmit array, by adjusting the amplitude and phase of current at each element, a homogenous  $B_1$  is created inside sample [19].

The proposed 3D-printed MTL resonators in this thesis can be used in transmit array configuration. 3D printing technology allows integrating the state of the art parallel plate capacitors to MTL resonator, therefore by matching the resonator to input impedance of power amplifier the amount of RF power required in transmit can be reduced. It has to be stated that using MTL resonators the coupling between elements in higher magnetic fields is reduced.

### **3.1.2 Volume Coils**

Volume coils are used for a specific region of the body or for the entire body, and they have shown better magnetic homogeneity than surface coils. In higher MR fields that higher SNR can be achieved, shorter wavelength causes some challenging issues and degrades the performance of conventional coil [20], [13], [21]. The issues that arise from higher magnetic fields are: non-uniform current distribution in the coil elements that reduces the homogeneity of transmit field; self resonance at frequencies lower than the operation frequency; and higher electromagnetic losses [20]. Using transmission lines with cavity elements is recommended as a solution for these issues [20]. Birdcage coils were introduced to enhance the transmit efficiency by their uniform transverse magnetic fields [22]. The cylindrical volume shape of this resonator allows quadrature excitation that reduces the RF transmit power and increases the SNR [13]. Birdcage coils are composed of wires or copper strips running along Z-direction (longitudinal axis), and the current is distributed as single cycle of sinusoidal on the surface of cylinder, which creates a uniform transverse magnetic field; the sinusoid current is approximated by discrete legs [22]. The coil is built as a network of inductors and capacitors distributed as low-pass, high-pass, or band-pass filter [22], [8], depending on the design and the location of these elements (capacitors). TEM coil is a transmission line coaxial cavity that resonates in a TEM mode [20]. Typically, in a TEM coil each strip is a resonant mesh that a current is given to, and because of the current mesh's boundary condition the distribution along the coil is sinusoidal. The distributed network, composed of transmission line and resonant cavities, has shown successful performance in higher field clinical applications [20]. Using quadrature excitation in TEM coil, maximum homogeneity for transmit RF field is achieved at frequencies of 500 MHz or higher [20].

### **3.1.3 Conductors and the Skin Effect**

At high frequencies, skin effect distributes the current only on the surface, and reduces SNR by increasing the resistance [22]. If a current is passed in the conductive wires, the skin depth can be shown as [23]:

$$\delta = \sqrt{\frac{2}{\omega\mu_0\sigma}} \quad (3-1)$$

in equation (3-1),  $\sigma$  is the conductivity of any conductor, and  $\mu_0$  is the free space permeability [ $4\pi \times 10^{-7} H/m$ ]. The conductor resistance in an alternating current increases with factor of  $\sqrt{f}$  [22], [23]. It has been recommended by authors in [23], that in order to minimize the resistance, the thickness of conductor must be six times greater than the skin depth of that conductor at the operating frequency. As one can realize from equation (3-1), by increasing the operating frequency, for instance to 200MHz, since the copper conductivity is constant, the skin depth value will decrease gradually. Also, it has been stated that in circular cross section conductors, if the resistance is minimized and the current density per unit of length of conductor is maximized, then the signal to noise ratio is increased [23].

### 3.1.4 Coil Conductivity Loss

It has to be noted that since the resistance of the RF coil varies inversely with the skin depth, the thickness of signal line conductor is recommended to be five/six times greater than the skin effect in order to compensate for skin effect [24]. Another factor that is considered in RF coil's resistance is its intrinsic thermal resistance, which can be reduced by cooling the coil or using superconductive material instead [25].

The inductor of the transmission line stores the magnetic energy which is needed for coil resonance [22], and its value depends on the shape and the cross-section of the conductor. The design of birdcage coil is sensitive to the element (capacitor) value selection, as such having small capacitances in the legs mandates large inductances that increases the voltage potential on them; this will increase the electric field produced in the sample that can become noise in receive mode or heat transferred to human body (SAR) [22]. When choosing discrete capacitors for design, few considerations should be taken care of: ESR (equivalent series resistance), voltage and current ratings, thermal coefficient, and series resonant frequency [22]. High ESR capacitors will degrade the SNR since they are lossy and

in turn they need high RF power transmission, which leads to temperature hazards in coil. The voltage rating is recommended to be high [22], in order to bear the transmission power.

### **3.1.5 Birdcage Coil Frequency Tuning and Impedance Matching**

The birdcage coil should be matched to Larmor frequency, and iterations (increasing and/or reducing capacitors) in elements must be applied in a way to retain the electrical symmetry of the coil [22]. The coil should be tuned in order to obtain high homogeneity in  $B_1$  for the 1<sup>st</sup> mode. Typically, variable and high Q capacitors are used to tune the coil's frequency [22].

Matching is required for the coil since it has to be connected to RF amplifier through coaxial cables which have nominal 50  $\Omega$  impedance. Baluns are used in birdcage coils to prevent common mode currents; one approach is that in birdcage coils, the shielding of coaxial cables can be connected to coil's shielding through a virtual ground [22]. The synthesis for birdcage coil impedance matching can be done with two different approaches which both rely on smith chart.

### **3.1.6 Microstrip Coils**

In array transceiver coils, which have proven potential for high SNR, homogenous  $B_1$  through the RF shimming, and parallel imaging gain, the decoupling between coil elements still remains an issue. Assuming a human head with a sample permittivity of 50, the wavelength in the sample is reduced resulting in RF inhomogeneity [26]. The capacitive shortened transmission line has been introduced as an effective way to reduce the size of transmission line resonator for RF coils, as well as being beneficial in achieving high transmit efficiency and parallel imaging performance [27], [11].

Authors in [26] designed an array transceiver MTL (microstrip transmission line) elements, where, by using the variable capacitors at the ends of transmission line, they have adjusted the electrical length of resonator, additionally reducing  $B_1$  variation across conductor length [28]. Typically, the coil should be matched and

tuned using variable capacitors and bench measurement is performed to make some small iterations in the matching. In order to map the transmit magnetic field efficiency, multiple images should be acquired.

In the transceiver coils, when sets of transmit and receive transmission lines are used, the isolation should be taken care of in order to avoid resonance shift. Hence, in some arrays, this has been done using decoupling capacitors between elements. In the designs of transceiver coils, the coil coupling can reduce the performance and the use of RF shield is necessary though having a trade-off on transmit efficiency [26]. The presence of PIN diodes in receive elements (for instance connection between the transmission line and the ground of coaxial cable) can increase the detuning between transmit and receive array [26], and the effect of decoupling is decreased during RF transmission.

The transceiver array coils use separate RF connection for each transmit element and thus their phase and amplitude can be adjusted. The loading conditions can affect the performance of the load in terms of matching and the resonance frequency. Therefore retuning and matching is necessary. Matching and tuning can be done before and after loading the human body.

Matching and tuning is critical in RF coils applications. Typically, fixed or variable capacitors are used in RF coils, and the price of high Q, MR compatible capacitors can be high. In this thesis, parallel plate capacitor model is integrated with MTL resonator as a new method to replace traditional matching/tuning capacitors. The 3D model of parallel plate capacitors provides a quick and easy iteration process by trimming the length or width of conductor of parallel plate capacitors.

A microstrip resonator model is demonstrated in [29], in which there's a matching capacitor  $C_m$  and a tuning capacitor  $C_t$  at one end, and a fixed capacitor at other end  $C_f$  that are used to tune and match the resonator to Larmor frequency.

Basically a MTL is composed of a signal line (acting as an inductor) laid on low loss material as dielectric, and by using capacitors, the electrical length of the resonator is adjusted to resonate at the desired frequency. The ground plane is a conductive layer of copper that is attached under the substrate. In Figure 3-2, a

single element of an array coil is shown with an automated circuit to match and tune the resonance frequency after loading. In Figure 3-3, the microstrip resonator is shown with matching and tuning capacitors at both ends [30].

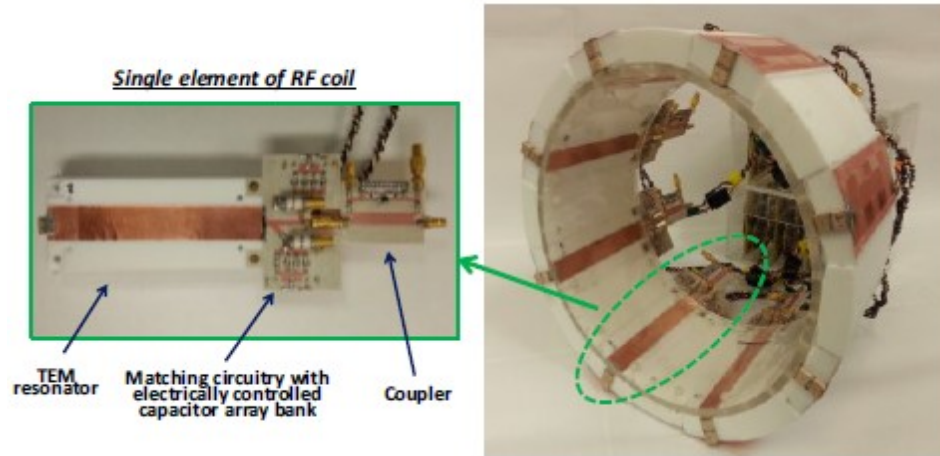


Figure 3-2: The 8-channel head coil and a single element shown composed of a TEM resonator connected to automated matching circuit [30], IEEE copyright line @ June 2013 IEEE.

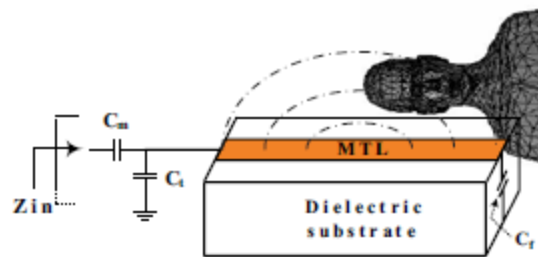


Figure 3-3: Microstrip resonator with matching and tuning capacitors at both ends [30], IEEE copyright line @ June 2013 IEEE

A typical MTL resonator is a microstrip transmission line in parallel with a ground conductor with a substrate as dielectric in between them. One type of MTL line is represented as sandwich MTL that has ground planes at both top and bottom of the microstrip. The MTLs with only one ground plane are called half-shielded [31], [32]. In the frequency range where the length of microstrip line is comparable to wavelength, the magnetic loss in microstrip line is the dominant factor in unloaded condition [31], and it is mainly dependant on the microstrip line's thickness. The size flexibility, simplicity of fabrication, and lower cost of MTLs are some of the advantages that promote these resonators to be used in MRI. It has

been shown that microstrip coils without RF shielding can be used for imaging while retaining high efficiency at high fields [28]. The length for half wavelength resonance of RF resonator is shown as:

$$l = n\lambda/2 \quad (3-2)$$

where,  $n$  is an integer and  $\lambda$  is the wavelength corresponding to the Larmor frequency [32]. The resonant wavelength of the microstrip coil can be shown as:

$$\lambda = \frac{\lambda_0}{\sqrt{\epsilon_{eff}}} \quad (3-3)$$

in equation (3-3),  $\lambda_0$  and  $\epsilon_{eff}$  are wavelength in free space and effective permittivity of the substrate. Then, if we assume  $W$  to be the width of microstrip transmission line and  $H$  to be the thickness of substrate, we have [32]:

$$\epsilon_{eff} = \frac{\epsilon_r + 1}{2} + \frac{\epsilon_r - 1}{2} \left[ \left( 1 + \frac{12H}{W} \right)^{-0.5} + 0.004 \left( 1 - \frac{W}{H} \right)^2 \right], \quad (3-4)$$

*for  $W/H \leq 1$*

and,

$$\epsilon_{eff} = \frac{\epsilon_r + 1}{2} + \frac{\epsilon_r - 1}{2} \left( 1 + \frac{12H}{W} \right)^{-0.5}, \quad (3-5)$$

*for  $W/H > 1$*

In order to test the resonator, a sample that mimics the human body is needed. As an example, in a gel phantom preparation an organic hydrophilic polymer, TX 115 gel is used as phantom in [32], and 20g of TX 115 powder was mixed with 200g deionized water at 6°C [32]. The solution liquid is mixed inside the 1000-ml beaker and stirred until it is dispersed in all the phantom and then vacuum is pulled onto the beaker to remove the air bubbles. The solution is heated inside water for 1h until the solution looked firm. This solution is changed to a gel in 24hrs. The microstrip resonator in [32] is a one square loop or two square loop resonator that is placed inside the magnet but the matching and tuning capacitors with an inductor are placed outside the bore using long coaxial cable.

Taking advantage of design and fabrication possibilities that are proposed in this thesis, the MTL design can be altered from Figure 3-3 to minimize the amount of dielectric used in MTL resonator, which in turn reduces the loss attributed to coil resistance. The proposed MTL resonator in this thesis uses mostly air-filled dielectric, thus in order to achieve that, iterations in the design have to be made. In this thesis, 3D-printing is introduced as a new manufacturing technology for MTL resonators. This technology allows one to build matching/tuning capacitors monolithically with the MTL resonators. It also proves advantageous in that iterations in the design aimed at specifically increasing performance are made feasible.

### 3.1.7 Performance Evaluation

In this section, the imaging acquisition parameters are introduced. Examples of imaging sequences from previous works are described. The performance evaluation for RF microstrip coil is also outlined.

In a microstrip resonator (MTL) coil, the  $B_1$  penetration can be calculated as the depth in the sample to which the signal amplitude drops to 5% of its maximum value [32]. In order to calculate the signal to noise ratio (SNR) a sequence should be given in transmit, for instance, for FID (free induction decay) the appropriate RF pulse with bandwidth and amplitude should be selected as such to maintain  $90^\circ$  flip angle inside the phantom. On the other hand in order to acquire image, few parameters can be chosen as those chosen in [32]: TR/TE=1200/10ms; acquisition matrix=128×128; FOV=12×12cm<sup>2</sup>; pixel size=0.8×0.8×1.5mm<sup>3</sup>; and number of slices = 64 as it was selected in MTL measurement set up in [32].

In order to generate the SNR image, a set of parameters can be selected as described when acquiring the pulse sequence (e.g., gradient echo) [26]: pulse bandwidth=300Hz/pixel; nominal flip angle =80°; voxel size = 1 × 4 × 4mm; and repetition time/echotime=8000/3.5ms. Then the signal amplitude at the center will be divided by the standard noise deviation.

The parallel imaging performance of each coil can be analysed using g-factor images, where in parallel imaging g-factor is calculated from the field of view (FOV) sensitivity profile (the ratio from an individual element over the root-sum-square of all channels), [26].

Then, in order to calculate SNR of the image, the data is analyzed in Matlab. Here,  $S$  as “signal” is the average signal intensity in the region of interest (ROI) of size of chosen pixels. Then  $\sigma$ , “noise”, is extracted as standard deviation of the pixel intensity, which is usually picked up from the image where the signal is zero and noise is located [32].

$$SNR = \frac{S}{\sigma} \quad (3-6)$$

The  $W/H$  ratio has significant effect on  $B_1$  penetration depth [32]; as an example of such effect, decreasing the ratio to 1 increases the penetration depth to its highest value. However,  $Q_{unloaded}$  decreases when  $W/H$  is reduced to 1 because the radiation loss is increased [32].

### 3.1.8 Transmit Efficiency and Loss

Since MTL resonators built in this thesis are meant to be transceivers, the transmit efficiency is a crucial parameter. The  $B_1$  power sensitivity is described as [33]:

$$S_{p0} = \frac{B_1}{\sqrt{P_0}} \quad (3-7)$$

which is related to the  $B_1$  transmit efficiency. This equation is used for unloaded coil. The sensitivity of a loaded coil is shown as [33]:

$$S_{pl} = \frac{B_1}{\sqrt{P_0 + P_p}} = S_{p0} \sqrt{\frac{Q_l}{Q_0}} \quad (3-8)$$

where  $P_0$  is the power dissipated in empty coil’s resistance or the resistance from the coil itself which is attributed to the substrate and conductor.  $P_p$  is the power dissipated in the sample or phantom in case of this thesis. The equivalent resistance of empty coils and phantom can be shown as  $R_0$  and  $R_p$  [33]. The sensitivity of

power is also described in terms of quality factor [34], [24]. The power efficiency of the coil is shown as:

$$\eta = \frac{P_p}{P_p + P_0} = 1 - \frac{Q_l}{Q_u} \quad (3-9)$$

The effective resistances in a RF coil itself is representing the random thermal motions of electrons in the coil and the radiation, emitted and absorbed by the RF coil [24]. On the other hand, the effective sample (phantom) resistance represents the inductive and dielectric coupling between the RF coil and sample [24]. Here, the losses in the RF coils and the losses that are considered as a result of coupling between sample and RF coils are described in detail.

In this thesis, six MTL resonators will be fabricated using 3D printing technology. Their performance in terms of transmit efficiency will be compared to a standard low loss Rohacell foam. It is proposed that using 3D printing, as a new fabrication method, iterations can be made in the design that will increase the transmit efficiency.

### 3.1.9 Radiation Losses

Losses due to radiation can be eliminated using RF shielding. These radiations are emitted and absorbed by RF coils [24], which cause variations in voltage across the coil. A variable resistance can characterize this effect [35], [24]:

$$R_{rad} = \frac{\pi}{6c^4} \sqrt{\frac{\mu_0}{\epsilon_0}} \omega^4 a^4 \quad (3-10)$$

here  $c$  is speed of light,  $\epsilon_0$  is permittivity of free space, and  $a$  represents the radius of a solenoid coil. In microstrip coils, leak of magnetic field occurs due to gap between the ground plane and the floating plane, which causes higher radiation, though decreasing this gap will reduce the radiation [36].

### 3.1.10 Homogeneity

A comparison between three volume coils regarding their  $B_1$  field homogeneity is shown in Figure 3-4.

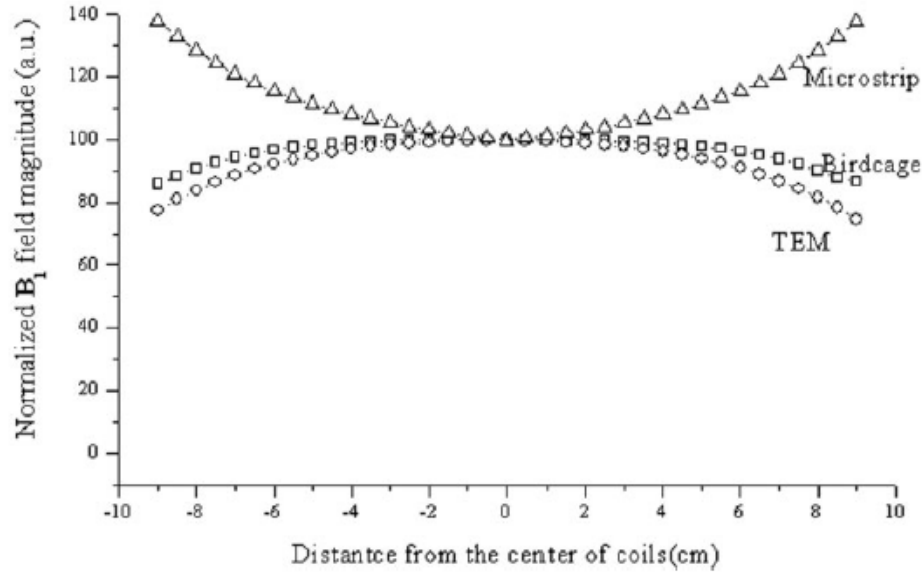


Figure 3-4: “Simulated  $B_1$  field distribution in the transverse direction for the unloaded volume coil.  $B_1$  field magnitudes at the center of all coils are normalized to 100%. The birdcage coil has better unloaded  $B_1$  field homogeneity than TEM and microstrip coils [36].

$B_1$  field homogeneity means having same flip angle in the entire sample. Also the receive coil is sensitive to the magnetization from entire sample. The results in [36] indicate that birdcage coil has better  $B_1$  homogeneity compared to TEM and microstrip coils. In Figure 3-4, the  $B_1$  field distribution is shown in central axial plane, and it has to be noted that the field of the microstrip coil is stronger in the periphery region compared to the iso-center of coils [36]. It has been stated that radiation loss of TEM is lower than microstrip and birdcage coils [36]. Moreover, it is shown that the microstrip volume coil is better in SAR and SNR compared to the other two.

It has been recommended in [24] that placing an RF shielding around the coil will reduce the radiation losses.

### 3.1.11 Dielectric Losses from Sample

The electric field of microstrip coil inside the sample produces a force on electrons in the sample. Hence this energy dissipates inside the sample and the overall dissipated energy is related to the effective resistance of sample [24]. The linear movement of electrons inside the sample, that is in parallel to the transmit electric field, creates a capacitive coupling between RF coil and electrons inside

sample [24], [34]. The equivalent circuit model is demonstrated for dielectric loss in [34], [25].

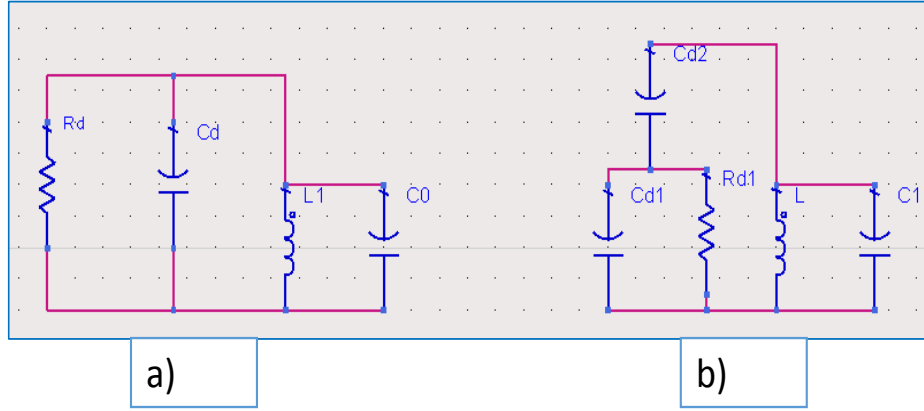


Figure 3-5: The circuit model with RF tuned to sample; a) RF coil inside the sample, b) RF coil separated from sample [32].

The equivalent series resistance is shown as [34]:

$$R_e = \tau \omega_0^3 L^2 C_d \quad (3-11)$$

here  $\tau$  is the loss factor in sample,  $L$  is coil's inductance and  $C_d$  is coupling capacitance between magnetic field direction and electrons. In Figure 3-5-a, the coil is assumed to be inside dielectric and the resistance  $R_d$  is modeling the loss associated with dielectric capacitance [34]. In NMR measurements, a lossy dielectric is inside the sample and always insulated from the RF coil. Therefore, Figure 3-5-b is representing the actual measurement set-up where  $C_{d1}, R_{d1}$  show the sample's lossy capacitance and resistance respectively, and  $C_{d2}$  is the lossless capacitance for the area of isolation between RF coil and sample. It has to be stated that RF coil has a parallel tuning capacitance with sample as it is shown  $C_1$  in Figure 3-5-b. The power loss in sample due dielectric loss was also derived in [37]:

$$R_d \simeq \tau \omega_0^4 L^2 R_{d1} C_{d2}^2 \quad (3-12)$$

at low frequencies as  $R_{d1} \ll 1/\omega C_{d2,d1}$ . This equation has a high frequency form as:

$$R_d \simeq \frac{\omega^2 L^2 C_{d2}^2}{R_{d1}(C_{d1} + C_{d2})} \quad (3-13)$$

in higher frequencies where  $R_{d1} \gg 1/\omega C_{d2,d1}$ .

The resistance of the sample,  $R_{d1}$  is proportional to the coil size and conductivity of sample [38]. The increase in sample conductivity and coil size geometry reduces the local Q factor. If high voltage potential difference exists across the coil, the dielectric decoupling loss is significant; reducing the potential difference across capacitors can manage the dielectric coupling between the coil and sample [24]. Also, in the case of solenoid coil, Faraday shields are placed between them to cancel out the dielectric coupling losses [34], [24].

### 3.1.12 Sample Inductive Loss

The transmit magnetic field of RF coil induces eddy currents in the sample, and in turn energy is dissipated in sample as heat [24]. On the other hand, eddy currents and random thermal motions in the sample will generate currents inductively in the coil [24]. As a result, the induced voltage is in shape of noise, which degrades the SNR and image quality. Based on the analysis in [34],  $R_m$  represents the effective resistance model for power dissipated in the sample from inductive losses [24]:

$$R_m \propto \omega^2 B_1^2 l b^4 \quad (3-14)$$

where  $b$  is the radius of a cylindrical non-magnetic sample and  $l$  is the length of solenoid coil [39]. As it can be seen the inductive loss has direct relation with the transmit magnetic field and inevitable in NMR imaging. The losses that are introduced in this section affect the performance of the RF coil. In this thesis, MTL resonator design is proposed since it has very low radiation loss in higher magnetic fields. If the transmit efficiency is high in a MTL resonator, the SNR of the image will be higher, but there are other factors that influence the SNR, such as flip angle, etc. The design of MTL resonator can be varied to increase the efficiency. The design steps for MTL resonators are described in Chapter 5.

### 3.1.13 Signal to Noise Ratio

The Signal to Noise Ratio for MRI coil is written as [40], [41]:

$$SNR \propto \omega |M_{xy} \cdot B_1| / \sqrt{4KT\Delta f R_e} \quad (3-15)$$

where,  $\omega$  is the Larmor frequency,  $B_1$  is the magnetic field,  $M_{xy}$  is the magnetization vector,  $R_e$  is the equivalent noise resistance, and  $\Delta f$  is the RF pulse bandwidth. The equivalent resistance can be shown as the summation of previous resistances:

$$R_e = R_{coil} + R_m + R_d + R_{rad} \quad (3-16)$$

The coil design must be as such to detect even a small signal from field of view (FOV) with least thermal noise.

### 3.1.14 RF Coil's Quality Factor

It is stated in [24] that the noise intrinsic to RF coils is difficult to measure. The calculation of energy loss in the coil and sample has been recommended as a straightforward solution to determine the thermal noise. The Q of a receive coil can be used as an indicator of sensitivity of the coil if the dielectric loss is considered to be negligible [13], [24]. In simple words, the ratio of total magnetic field energy of RF coil per energy loss during oscillation is called quality factor [24]. Therefore, quality factor can be used to determine the energy loss and noise. If a coil is tuned to Larmor frequency, then the quality factor is defined as [24]:

$$Q = \frac{\omega_o L}{R_e} \quad (3-17)$$

where, the inductance of the coil is shown with  $L$ , this equation in the case of unloaded Q will be:

$$Q_u = \frac{\omega_o L}{R_u} \quad (3-18)$$

where  $R_u = R_{coil}$ , and in a loaded case:

$$Q_l = \frac{\omega_o L}{R_l} \quad (3-19)$$

where  $R_l = R_{coil} + R_s$ . In the unloaded case, the resistance is only due to the contribution of coil. However in the loaded case, contribution from the sample is added.  $R_{coil}$  is due to ohmic loss but  $R_s$  is the resistance model for electromagnetic losses of magnetic energy inside the sample. It has to be noted that Q information

cannot be used to determine the SNR for a coil since both noise and signal change in linear fashion with Q [42], [24].

In case of unloaded Q, resonator is placed on the bench and Q is measured, but in loaded case the resonator is placed on phantom, as it was shown in Figure 5-12, and Q is measured. An important parameter that can be achieved from Q information is Loading Factor (LF) [24]:

$$LF = 1 - \frac{Q_l}{Q_u} = 1 - \frac{R_u}{R_l} \quad (3-20)$$

The loading factor provides information to investigate the performance of each coil under testing.

$$LF = \begin{cases} 0, & R_s \ll R_{coil} \\ 0.5 & R_s = R_{coil} \\ 1, & R_s \gg R_{coil} \end{cases} \quad (3-21)$$

when  $R_s \ll R_{coil}$ , the coil resistance dominates the losses that are absorbed from sample, therefore the coil does not detect any useful signal from sample. At the cross over point, where  $R_s = R_{coil}$ , there is equal contribution from both sides.

When  $R_s \gg R_{coil}$ , the losses from sample dominates over the losses from the coil. This value of LF of coils is also called the efficiency of the coil.

The transmit efficiency or power efficiency in the equation (3-9) is maximized if the received signal is dominated by losses from the sample, and that is equivalent to maximizing signal to noise ratio in receive coil, where the effective resistance is not dominated by coil's resistance [43], [44].

In this thesis, Q measurement is performed on the bench for six MTL resonators. There are two available methods for Q measurement, and they are described in the next section. Based on Q measurement, we can predict how much loss is being detected from sample by the MTL resonator. If the loss from sample dominates the loss from MTL resonator itself, a good SNR value will be achieved. Based on information provided in this chapter, Q and SNR values for six MTL resonators are investigated to characterize the performance of MTL resonators made by 3D printing.

### 3.1.15 Methods for Measuring Q

Method-1: In [43], a method is described to measure Q factor of coils with transmit and receive loop pick up probes. A synthesizer, and a meter or oscillator pick-up loops are used to measure the Q in high frequencies. The RF coil in this case is “symmetrically and loosely” coupled to two probes at each side [43].

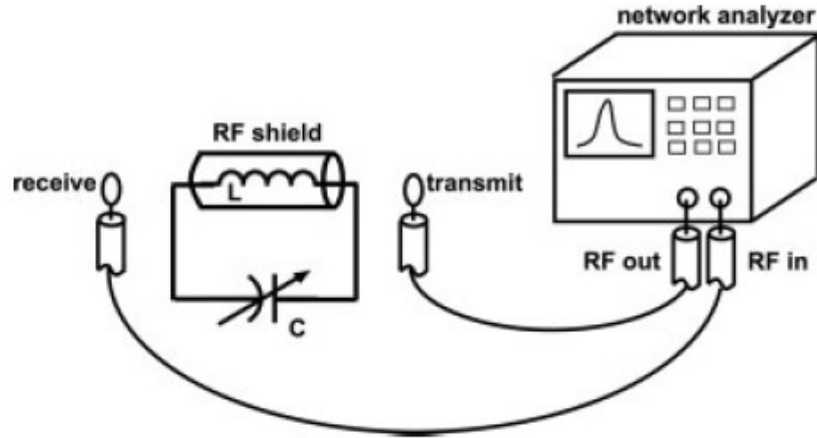


Figure 3-6: measurement set-up as method to measure Q factor. Probes are placed at both sides orthogonal to  $B_1$  field [24]. The above setup is for the unloaded case.

The  $S_{12}$  (dB) is used to measure the Q factor and -3dB point is determined using bandwidth markers. The set-up shown in Figure 3-6 is repeated for each coil at loaded and unloaded cases and data is recorded for each coil. The Q can be measured from -3dB of the peak value of transfer function as:

$$Q = \frac{f_0}{BW(3dB)} \quad (3-22)$$

Method-2: In this method, Q factor is measured using coaxial cable connected to one port of VNA and one pick-up cable connected to the other port [45]. In this method the pick-up loop is used to measure the frequency response from the resonator. The Q measured with this method uses half-power bandwidth, then by knowing the reflection coefficient at the resonance, it can be determined whether the RF coil is under-coupled or over-coupled. For calculation with this method, real and imaginary parts of  $S_{11}$  is measured and its magnitude  $\rho$  is calculated.

$$K = \frac{1 + \rho}{1 - \rho} > 1 \quad (3-23)$$

$$K = \frac{1 - \rho}{1 + \rho} < 1$$

in equation (3-23),  $K$  is the coupling factor,  $K > 1$  is used when the sample (loaded) condition improves the matching of resonator (over-coupled) and  $K < 1$  is used when resonator's matching is degraded by introducing the sample (under-coupled) [45]. Using the set-up in method-2, the  $Q$  value is recorded as  $Q_{measured}$ , and then the  $Q$  of the coil can be calculated:

$$Q_{coil} = (K + 1)Q_{measured} \quad (3-24)$$

In this thesis, for six MTL resonators the  $Q$  is calculated using this method and efficiency values are driven. MTL resonators in this thesis are fabricated using 3D printing technology and their performance is compared to standard low loss foam resonator. Based on their performance, if the results show acceptable performance, 3D printing can be adopted to manufacture MR compatible coils.

### 3.2 Additive Manufacturing

Additive manufacturing as an emerging technology is replacing traditional fabrication methods for a variety of products to significantly lower the cost and labour, e.g., it can be used to make custom-built MR compatible coil prototypes. It has recently been shown that 3D printing of polymer substrates and silver nanoparticle inks can be used to develop RF devices. Unlike traditional machining techniques, which create the object by drilling or etching to remove and shape materials, 3D printing generates three-dimensional objects from a computer model by laying down successive layers of structural material. In comparison to conventional manufacturing techniques, rapid prototyping technology fabricates 3D models using layered manufacturing process where the additive layers are laid down on each other and bond in one direction [46]. One main benefit of additive manufacturing is that the steps required for fabrication are minimized since a 3D CAD model is directly built in the 3D printer. Typically, copper tape is used in RF coils as conductive material. In an advanced approach, we propose to build MTL resonator's substrate and conductive layer in one single run with 3D printer.

### **3.2.1 Photopolymer-based Systems:**

This system uses a vat of photopolymer resin, and a model is fabricated out of it. In this method, liquid is used to form parts. The advantages of this model is that its accuracy is good, and layer fabrication is very precise. This method has shown poor material properties such as temperature resistance and mechanical strength compared to materials fabricated with other AM methods. A UV light cures the resin layer by layer. Some systems use a blade to make the surface of layer smoother for better layer bonding. There is a need for support material in fabrication phase. This process uses plastics and polymers. UV-curable photopolymer is one type of polymer that is frequently used in this process. Advantages and disadvantages of different AM systems are listed below [47].

Advantages:

- High accuracy and good finish
- Relatively quick process
- Larger build area

Disadvantages:

- Expensive
- Limited material use of photo-resin
- Requires lengthy post processing for parts

### **3.2.2 Powder-based Systems:**

Powder-based systems deposit a bed of powder layer by layer. The deposition process uses a laser or electron beam to melt and fuse the material. This process doesn't require support material, but for some metals, the use of support is essential. All techniques in this category are associated with deposition of powder material on previous layers. A roller is used to deposit new layers and then this layer is fused to the previous layer. The powder-based mechanism is used in Direct Metal Laser Sintering (DMLS), Electron Beam Melting (EBM), Selective Heat Sintering (SHS), Selective Laser Melting, and Selective Laser Sintering (SLS). In this process, material properties can change subject to how many times material has been reprocessed in the bed. Temperature and powder bed settings are important parameters that influence the deposition in SLS process. DMLS is similar to SLS

but it used metals instead of plastics. The accuracy and finish of printed parts depends on the particle size of powder [47]. The powder-based process uses any powder-based material and polymers. SHS uses Nylon. SLM, SLS, and DMLS use Stainless Steel, Titanium, Aluminum, Cobalt Chrome, and Steel. EBM uses titanium, copper, and Cobalt Chrome.

Advantages:

- Relatively inexpensive
- Suitable for visual models and prototypes
- Shorter post-processing time that allows faster fabrication
- Large range of material available
- Powder perform like an integrated support for the structure

Disadvantages:

- Size limitation
- Higher fabrication time since pre-heating and cooling-down cycles are needed
- Inferior accuracy and finish compared to photopolymer-based systems
- Huge power usage

### **3.2.3 Molten Material Systems:**

All systems that use molten-based process need support material. Material is drawn through a nozzle on print-bed layer by layer. Deposition Modelling (FDM) is a common method in this category that is based on extrusion mechanism. In this method, the support material can be generated automatically or by the user with some flexibility. FDM is similar to other AM methods, as it deposits the model layer by layer, but on the other hand it is different since the material flow is with a constant pressure to reassure a high accuracy. The shape of printed part in FDM depends on nozzle, acceleration and deceleration, and viscoelastic characteristics of materials. This category of AM uses plastics and polymers such as: Nylon, PC, ABS, and etc. FDM's speed depends on the feed rate and plotting speed.

Advantages:

- Inexpensive process
- Easily accessible material like ABS with good mechanical properties

Disadvantages:

- The nozzle radius limits the final quality
- The accuracy and speed is low compared to other AM processes
- In FDM machine all nozzles are circular and drawing a sharp edge is impossible

### **3.2.3.1 Extrusion-based system**

The material is restored in the form of a pellet, powder or continuous filament. Materials are forced through an extruder nozzle by applying pressure. If the applied pressure remains constant throughout the printing process, the cross-section of the extruded layers will be constant since the flow rate is constant. Material is in semi-solid state at the nozzle output. When a layer is completed, the extruder moves up one index to print next layer, alternatively the print bed can be moved down.

There are two main process categories for extrusion-based systems: temperature based extrusion systems, and chemical based systems. In temperature based process the material is kept molten in a reservoir and can flow out from nozzle. In this model the extruder is mounted vertically. In the second form, chemical change yields to solidification. A curing agent, residual solvent, or drying with air allows bonding to happen.

#### **Material Loading:**

Extrusion system usually uses a chamber for materials. The chamber contains a reservoir to keep the molten material. If material is in the liquid form it can be pumped to chamber. For other materials such as pellets and continuous filaments, screw feeding is used. Screw feeding has enough pressure to push the filament inward into the extruder.

#### **Liquid Formation:**

The bulk material is fed to the chamber and heated using heating coils that are wrapped around the reservoir chamber. Liquid material is pumped directly to the chamber. The heating process has some issues regarding the size of chamber. As the chamber size becomes larger, the uniformity of heating process gets more

challenging because of heat transfer, presence of thermal currents in the melt, and the location of heat sensors. Another limitation regarding chamber heating is that material should be kept at the lowest possible temperature since some material can degrade at high temperatures or they can burn inside chamber. The burnt residues inside chamber will contaminate the next filaments.

### **Extrusion:**

The extrusion nozzle is the part that determines the size and diameter of the printed lines. Larger diameter for nozzle allows higher flow rate but lower precision. Twice the diameter of the extruder nozzle can be chosen for minimum thickness in order to maintain the accuracy. The pressure difference between chamber and environment controls the flow rate of material from nozzle. Flow depends on pressure drop, nozzle geometry, and material viscosity. Screw helps material to flow inside the chamber and the pressure drop causes the material to flow out through the nozzle.

### **Solidification:**

Parts are printed on the surface of print bed. The surface tension of print bed and gravity can affect the geometry of printed parts. If the extruded material from the nozzle is in molten form, it can shrink in size when cooled. Hence, an enclosed environment with constant temperature can save printed parts from failure. Moreover, heat bed temperature must be kept constant since good amount of adhesion is required for first layer to bond to the heat bed surface.

### **Bonding:**

In the extrusion systems, the incoming layer (material) from nozzle must have adequate heat to activate the surface of previous layer in order to make good bonds. Gel based systems contain solvents or wetting agent inside the extruder to assure high strength bonding between new layer and adjacent layers. In both systems, energy must be given to previous layer. If this energy is not adequate, the layers will have separation in between.

### **3.2.4 Technology Overview**

AM technology has been introduced to a wide range of industrial and research fields and still continues to expand its applications. Additive manufacturing technology fabricates 3D physical model of a product from a solid computer model, in which the layers are stacked to form the desired shape. Large variety of 3D printing technologies have been introduced with their advantages and disadvantages depending on applications [48]. Fused deposition modeling (FDM), and selective laser sintering methods has been used to print dielectric substrates. Electron beam melting [49], and selective laser melting [50] are substantial methods for metal printing. In Electron beam melting printer, a high power electron beam is used to sufficiently heat in order to make bonds between metal particles in metal powder. Depending on the particle size, in this method, the surface roughness can be an issue in higher RF frequencies [48].

Among 3D printing technologies, FDM [51], [46] and inkjet printing [52] have the advantage of some degree of freedom in comparison to selective laser sintering [53], since the material is fed through a nozzle as opposed to selective laser sintering that needs a powder bed or Stereolithography that uses a vat of resin [51]. In FDM the print head or nozzle can be used to print on any geometry. Also, the long nozzle tip can enhance the capability of printing some angles on a substrate [51]. Each type of 3D printing technology has its own limits and advantages. For instance, inkjet printing provides high resolution compared to other methods but has constraints in type of material. Since the extrusion system uses heat to melt the filaments in the FDM process, thermoplastic materials can be used for printing. These thermoplastic materials have high molecular weight and can be structurally strong.

### **3.2.5 Material Properties**

The material used for MRI coils are rated with UL94, which is a test protocol that classifies laminates based on their resistance to flame [54]. The UL94-V0 that classifies the material based on their self-extinguishing property (very low burn time on vertical sample) [54]. Typically, the substrate material used in MRI coils

are extremely low loss foams with loss tangent  $< 0.0002$  [55]. Typical tensile strength for low loss foam is 1 MPa [55]. In this thesis, 3D printing thermoplastic materials are used to fabricate MRI coils. These materials are polymers, which are long chains of molecules and their intermolecular bonds weaken by applying heat. There are two temperature states: the glass transition temperature,  $T_g$ , and the melting point,  $T_m$ . For specific 3D printing polymers, these material's physical property will change, without any phase change, if the temperature is increased or decreased between these points. Some commonly used thermoplastic materials are - acrylic, which is a polymer called poly (methyl methacrylate) (PMMA) that is used as sturdy substrate for glass and other uses; ABS( Acrylonitrile Butadiene Styrene), which is a terpolymer, synthesised with styrene and acrylonitrile in the presence of polybutadiene and has shown high impact resistance and mechanical ruggedness; PC (polycarbonate), a material formed by condensation polymerization that is used in automotive, aerospace, medical and many other applications because of its high durability, exceptional accuracy, and superior mechanical properties; nylon™, which falls in the category of polyamides; polypropylene, which is mainly used in reusable plastic containers or microwave containers and polyester; poly lactic acid (PLA), which is a biodegradable thermoplastic that is driven from renewable resources. PLA is a polyester, and not a polyacid.

Since the material used in 3D printing is mostly thermoplastic material, the temperature has to be noted as a critical parameter in the process, because the heat can considerably affect the flow and shape of the material flow from print head.

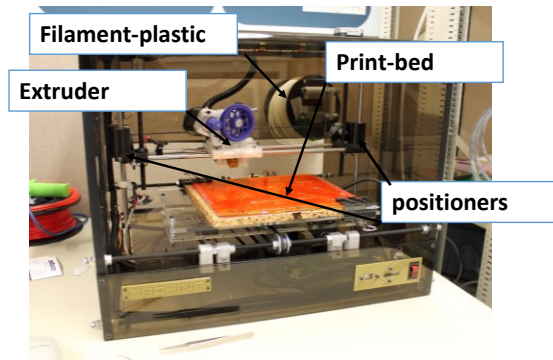


Figure 3-7: Desktop 3D printer at M2M laboratory- The University of Alberta



Figure 3-8: Commercial FDM 3000 system [51].

In Figure 3-7, the desktop 3D printer is shown with different parts labelled. There are three motors to move the nozzle (extruder) in the x,y,z directions. Fused deposition modeling is an additive manufacturing technology used in modelling, prototyping and fabrication. The fabrication process involves laying down layers of plastic filament. In Figure 3-8, the commercial FDM printer is shown. In [51], a development process is described to make printing, outside the chamber, possible. The additive layer deposition process is done by modifying the FDM printer such that the extruder moves up as the material height increases at each cycle of print, preserving the layer by layer printing concept. The print software requires x, y and z starting coordinates before each print, making operations such as pausing, stopping, and restarting, possible [51].

To begin with, the FDM printer parts (i.e. print-head, printbed, and filament flow) must be calibrated. An important initial step is to adjust the print bed's temperature to assure a uniformly heated bed; a lack of uniform heat will degrade

the bonds of the first layer and the possibility of having separate layers or gaps will be higher.

### 3.2.6 Challenges

**3D printers have energy inefficiency problem:** 3D printers use more energy to print plastic materials compared to the conventional methods such as injection molding. Laser metal deposition uses higher amount of electricity in comparison with traditional machining.

**Material:** AM has been developed for polymeric material, waxes, paper-laminates, composites, metals, and ceramics. CNC machine products are homogenous and have high quality. Parts that are fabricated with AM have some voids and anisotropy that can be result of part orientation, process parameters, and data communication with 3D printer.

**Material Bonding:** In inkjet printer, vaporized ink makes adequate bonds to paper. In 3D printing with extrusion system, the extruder uses a wetting agent to make sure the extruded layer bond to the adjacent layer. This is basically the energy that is delivered to material. If this energy cannot yield sufficient energy to the material, the additive layers can get separated or become non-uniform. A possible solution for layer bonding is to improve it by using an ultraviolet lamp to heat the layer. After each layer is extruded on the heat bed, an ultraviolet lamp passes over the layer; this improves the layer bonding strength. Too much of energy can cause underneath layer to flow.

**Heating chamber in extrusion-based systems:** Chamber is heated to melt the material and heat sensors are used to read the temperature. As the size of chamber gets larger, the control of heating system becomes more challenging because of heat transfer and thermal currents inside the melt.

**Solidification issues of material:** When a line is printed on the print bed, it must stay as it is designed, but factors like gravity and surface tension may degrade the solidification. Also size and geometry of a line can vary based on the environment temperature.

**Clean-up and post-processing:** After the part is printed, it must be cleaned to be ready to use. Some 3D printers use support material in printing process to make complex structures such as a cantilever beam and the support material can be cleaned after, to release the beam. Parts might also be weak at this step, hence a clean-up step must be done carefully and this requires time and experience.

**Speed of fabrication:** Additive manufacturing is a single stage process compared CNC machining, which is a multistep process.

### **3.2.7 Shortcomings and Objectives**

There is not a low cost 3D printer that can print plastic materials and metals in one machine. That limits the fabrication either to plastic or metal materials. In this thesis, for first time, a low cost 3D printer that only was capable of printing plastic material is modified to add conductive ink printing capability to it, doing so a low cost machine can print plastic and metal. In this thesis, the modification process is described in detail.

In this thesis, 3D printing is used to 3D-print state of the art MTL resonators with integrated parallel plate capacitors for MR applications. This technology offers the early design iterations to reduce the amount of dielectric used in MTL resonators to increase its efficiency and SNR. 3D-printed parallel plate capacitors eliminate the labour-intensive work of soldering for matching/tuning capacitors.

## **Chapter 4    3D Printing and Applied Modifications for MRI RF Coil Printing**

This thesis investigates 3D printed MRI coils for applications as custom designed MR compatible coils. In this thesis, three different materials for 3D printer are used to fabricate MTL resonators and have been characterized for their RF performances in MRI environment: (1) Polylactic Acid (PLA), (2) Acrylonitrile Butadiene Styrene (ABS), and (3) UV-resin (Objet Verogray RGD850, Stratasys). Copper tape and conductive silver ink (Ag-610, Conductive Compounds) is used for conductive lines and ground layers for these resonators, and their performance is compared to a standard MTL resonator made with copper strips on low loss foam substrate with same dimensions. In this thesis, 3D printing is used to build the entire MTL resonator including matching capacitors monolithically in one step, eliminating off-chip capacitor integration; thus reducing the time and cost significantly. The next sections will focus on the resonator design and the material characterization.

### **4.1 3D Printer Modification Process and Fabrication**

This thesis shows that 3D printer can be used to fabricate custom designed MRI coils for various parts of body. To implement the project, two types of 3D printer are used: a desktop FDM 3D printer (X-series, Machina Corp Figure 4-1), and Objet Eden350V (Stratasys). The 3D desktop printer is capable of printing two different materials on the print bed: ABS and PLA, which are both thermoplastic materials, meaning, that they become mouldable when heated and solidify when cooled down. The 3D printing process is done by successive laying down of the material. The Objet printer can print the material called UV-cured resin (Objet Verogray RGD850, Stratasys) and uses a sacrificial support material to infill the empty spaces between posts. This support material can be etched using tweezers afterwards and the residue is washed away using acetone or water.

In order to print substrates with Objet Eden350V (Stratasys), the printer that can print UV-resin or desktop printer (PLA, ABS), a .stl file should be generated from 3D model of resonators. Then machine language g-code corresponding to layer dimensions is generated from .stl file. G-code is composed of all coordinates for layers of 3D model and based on g-code coordinates, the 3D printer will lay the material down on the print-bed to form the final prototype. Both of these 3D printers are only equipped for polymer printing. For the metal traces required on MRI coils, two techniques are investigated. Once copper tape is used to lay the ground plane and the metal required for signal line. In this thesis, it is proven (the results will be shown in the next chapter) that the concept of 3D printing using low cost copper tape can be used as comparable performance to standard MTL resonators built with low loss foam. As another easy and automated fabrication technique, metal ink 3D printing is developed and used. Therefore, the low cost 3D printer (X-series, Machina Corp) is customized to also include metal printing. In this section, the modification process of 3D printer which enables it to print conductive ink as the conductive material on substrates, is explained.

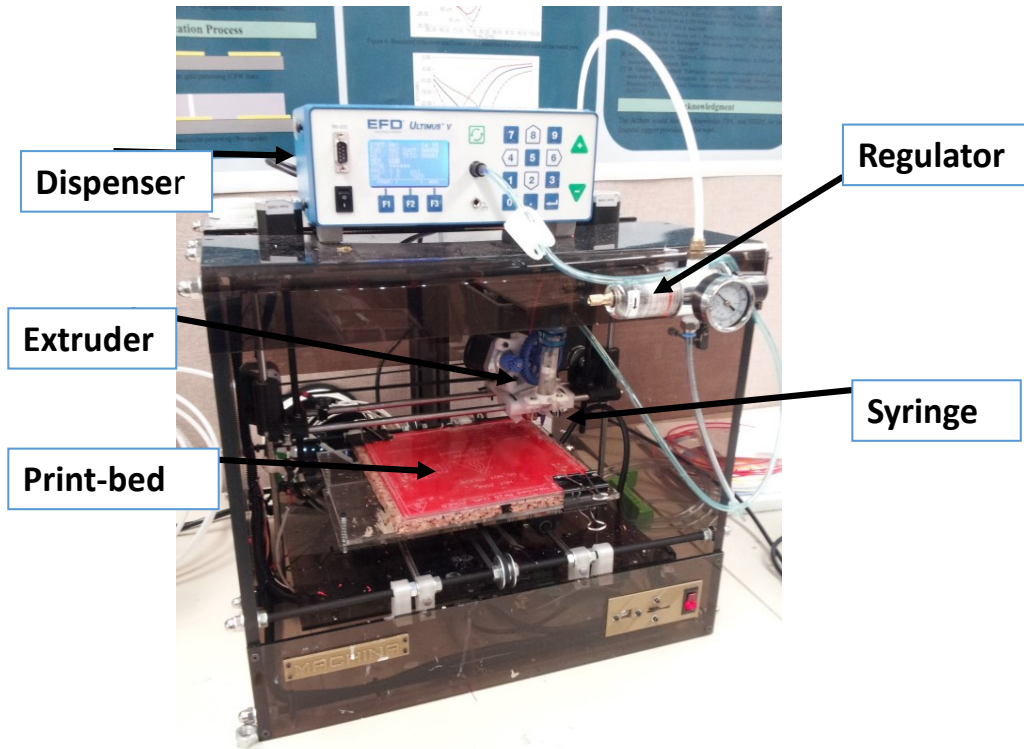


Figure 4-1: 3D desktop printer (X-series, Machina Corp, located at the University of Alberta, Electrical and Computer Engineering Department) is retrofitted with Regulator, Syringe, and a Dispenser (Ultimus V, Nordson) to print lines of conductive ink on the substrate.



Figure 4-2: Objet Eden350V (Stratasys) that prints UV-curable resin. It is located at Mechanical Engineering department, University of Alberta.

In order to add dispenser to 3D printer, the dispenser requires 120-125 psi clean air and it is recommended by company to use a compressor. Our lab is supplied with compressed air output by nanoFAB, and has been used as input to the air regulator. The regulator is adjusted to 100 psi in order to satisfy continuous flow of ink. Other side of regulator is fed to the behind panel of dispenser as the air input. The output of dispenser in front panel is connected to the syringe.

#### **4.1.1 Ink Printing Process**

Here, the 3D printing facilities available at the M2M (Microwave to Millimeter-Wave) lab of the University of Alberta are demonstrated. For the printing process, the required 3D printing software settings are outlined here, along with description of the 3D printer code modification steps. Previously, it was shown that silver nanoparticle ink can be used for 3D printers for one step fabrication of RF devices [56], [48], though the method of fabrication was not presented in [56]. As it is shown in Figure 4-1, in order to retrofit our desktop 3D printer to print lines of conductive ink we developed a new process involving: (1) air regulator, (2) 3D printer, (3) dispenser, and (4) syringe.

The printer is also using a software named Slic3r [57]. This software is modified to adapt to our needs. In the Slic3r software, a 2D model of the design is shown and printer parameters such as filament flow, home coordinates (needed to calibrate the printer as starting point), infill density, and temperature can be set. There are two softwares involved in 3D printing of models: (1) Slic3r, and (2) Repetier-Host. Slic3r is free-source software that is being used to create so-called “g-code”. Repetier-Host receives the “g-code” generated by Slic3r and sends it to a built-in microcontroller in the 3D printer, which sends the corresponding commands to motors, relays, and heaters.

There is a two-way communication bus between Repetier-Host and the microcontroller which sends back logs of the command line at each time a command is executed. Slic3r software cuts the 3D model into slices of paths for the extruder of the 3D printer to fill in.

This software, Slic3r, provides options such as speed, scale, infill, skirt and brim, layers and perimeters, to modify the g-code before extracting it. For instance, one can adjust the g-code to have a skirt (printing of a few layers surrounding the print area). A skirt provides the possibility to pinpoint the printing area if the object needs to be rotated and realigned for further ink printing. The first layer's and additional layers' heights determine the number of times that the extruder prints the support for infill at each layer as specified. One important parameter in the Slic3r settings is the extruder speed, which should be kept low since the perimeter and first layer act like a foundation for the 3D model.

In addition, the temperature of the extruder and print-bed can be adjusted from Silc3r. ABS is an amorphous material. In ABS printing process, the glass transition point is 105°C, and the print-bed temperature is kept around 80°C to ensure adhesion between ABS and print-bed. For printing the PLA material, since the melting point is 150-160°C, the print-bed temperature is kept around 60°C to provide adhesion to print-bed, although, heat is not necessarily required for PLA.

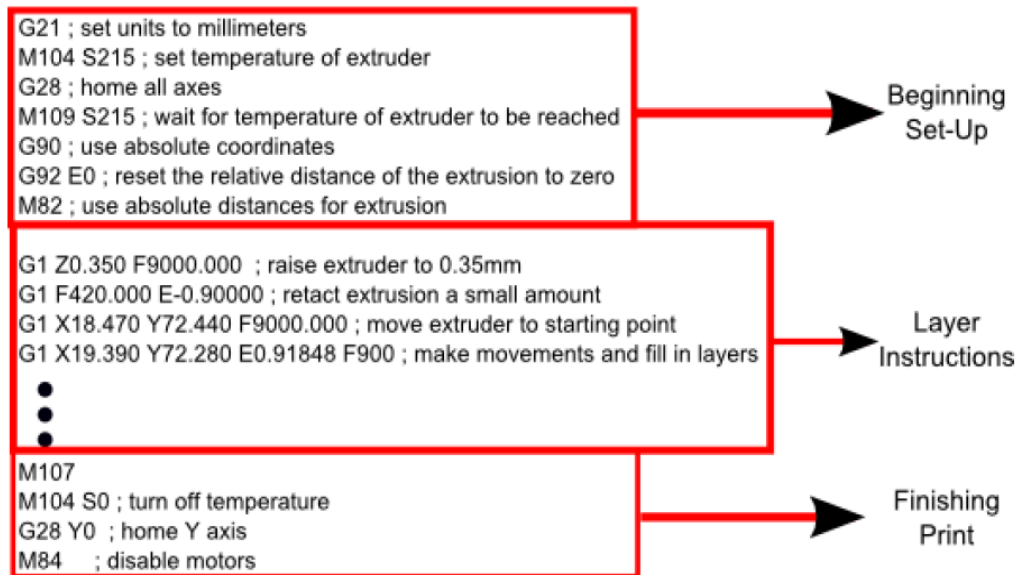


Figure 4-3: G-code example for substrate printing.

In Figure 4-3, at first, the temperature settings and coordinate calibration are sent to the extruder. Then the print path instructions for the layers are provided from

Silc3r program. Then the g-code ends with turning off the bed and extruder temperature, and homing all axes.

#### 4.1.2 RF Coils for Print

The modification to low cost 3D printer is done to add ink printing capability. In Chapter 5, the performance of ink printed MTL resonators will be compared to standard foam MTL resonator in MR applications. In the case of resonator with ink as conductor layer, ink printing process is done in 3 stages: (1) ground plane, (2) signal line and capacitors, and (3) two vertical walls. The full view of MTL resonator is shown in Figure 4-4. As shown in Figure 4-5, the resonator is split into three sections and printed separately. In the model of Figure 4-5, the plastic (substrate) material and ink parts are shown in green and red, respectively.

The ground plane and walls are printed on the print-bed with skirt. For capacitors, top plates and bottom plates have to be ink-printed, as it is shown in Figure 4-5. First, the signal line with capacitors is printed with skirt in the flipped position. HFSS software is used to model capacitors for the ink and dielectric layer separately, and then the .stl files are exported.

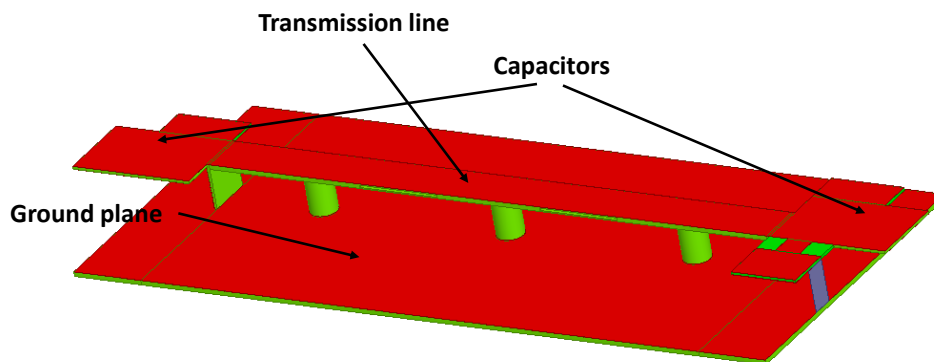


Figure 4-4: Schematic view of a full MTL resonator

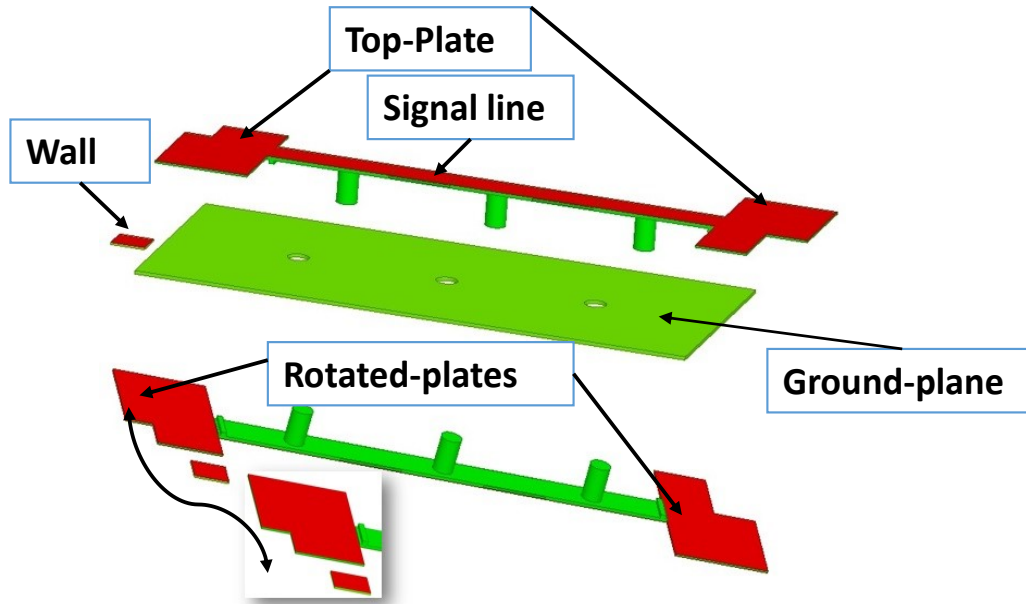


Figure 4-5: Resonator printed in sections of three, prepared for ink process.

In the Slic3r program, the printing speed must be set to low since the ink flow is low compared to plastic material. It is then adjusted according to the viscosity of the material. Next, the first layer should be set to be completely filled. In this case 10 mm/s has been used as the printing speed. The extruder temperature is then removed. The layer of ink on both of the end capacitors is adjusted to the minimum layer thickness of 0.2 mm. In our process, silver ink (Ag-610, Conductive Compounds) is used for conductive lines, capacitor plates, and ground layer. This ink is dried at room temperature for 5 minutes, or is dried by forced air. In order to be cured, it is either heated on the heat bed until the temperature limit of PLA (60°C) or ABS (100°C) is reached. This process of curing is repeated and the resistivity of the ink is measured. The sheet resistance measurement for conductive ink is done using a four point probe, the details of which is explained in section 4.1.3.

Afterwards, the resonator is flipped and placed inside the dimensions of the previously printed skirt. This time, since the printer prints the transmission line between the matching capacitors and top plate of the capacitors, one channel can be modelled with a width that is double the height of a layer to print the layer on the signal line (using one perimeter). This can be done alternatively by modeling a signal line with a width of 1 cm connected at both ends to capacitors. It has to be noted that the 3D model of the layer is given to Slic3r along with the offset between

extruder and syringe. In this way, by cancelling the temperature and including the g-code modification shown in Figure 4-6, the filament is not printed, and the syringe is used to print the ink. In Slic3r, since the height is increased to the offset of the printed resonator, the syringe tip should be placed slightly higher than the extruder to not collide with the printed resonator. Offset coordinates are calculated and incorporated into Slic3r ahead of printing.

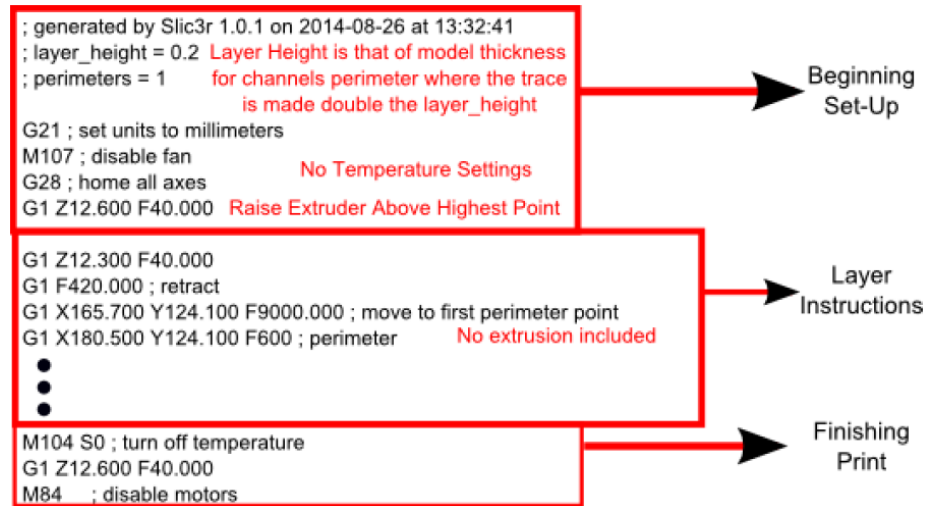


Figure 4-6: G-code modifications for ink printing, no extrusion required. Syringe and extruder are raised above the surface.

The Ulitimus V (Nordson) dispenser is used with  $600\mu\text{m}$  diameter syringe tips, this varies depending on the ink properties and its viscosity. With nanoparticle inks, smaller diameter syringe tips can be used. The pressure in dispenser was set to 9 psi for the initial flow (since ink might clog inside the tip and this can be reduced with high pressure) and 5 psi for normal continuous printing. Following these steps, the conductive silver ink is printed on two resonators substrates PLA and ABS. The RF performance of 3D-printed resonators will be investigated in the next chapter.

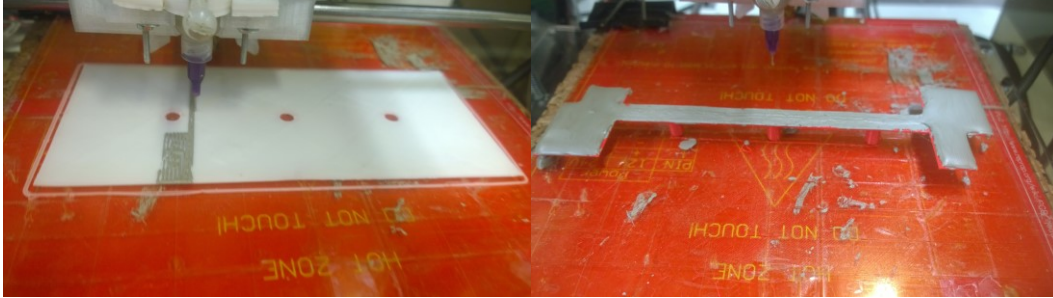


Figure 4-7: 3D printing ink on resonator parts, (a) ink printed on PLA resonator with capacitors on both ends, (b) ink printing on ABS material as ground plane.

### 4.1.3 Ink Resistivity Measurement

The resistivity of silver ink is measured on a glass substrate. The ink is dispensed and dried at the room temperature, and Four-Point Probe (Pro4 4000, nanoFAB, at the University of Alberta) is used to measure the sheet resistance. A fixed current is injected into the substrate via the outer probes and voltage is measured between the pair of inner probes. The spacing between the 4 probes are  $s_1=s_2=s_3$ . The advantage of this measurement is that it eliminates the contact resistance from the measurement and directly provides the sheet resistance of the conductive ink.

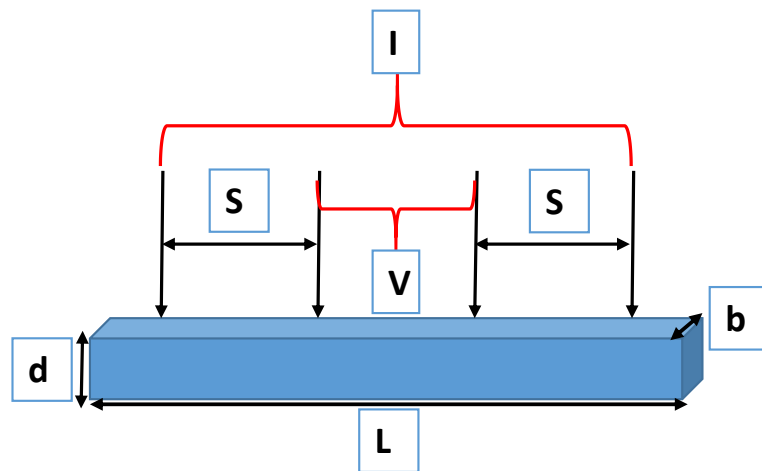


Figure 4-8: Four point probe used to measure the sheet resistance

The equation below is used to measure the sheet resistance in the four point probe [58]:

$$R_s = \frac{\pi}{\ln 2} V/I \quad (\Omega/\text{square}) \quad (4-1)$$

The thin film sheet resistance for the surface shown in Figure 4-8 is defined as:

$$R_s = \frac{\rho L}{d \times b} \quad (4-2)$$

if  $L=b$ , the sheet resistance for the square section is:

$$R_s = \frac{\rho}{d} = \frac{\Omega}{\text{square}} \quad (4-3)$$

and the resistivity in the four point probe is defined as:

$$\rho = \frac{RA}{L} \quad (4-4)$$

in equation (4-4),  $\rho$  is the bulk resistivity in ohms-m, R is electrical resistance, A is the cross sectional area, and L is the length of the material.

Table 4-1: Thickness and sheet resistance values of measured lines

<i>Ink line area</i>	<i>Thickness (<math>\mu\text{m}</math>)</i>	<i>Measured value <math>R_s</math></i>
$L=2\text{cm}, b=1.1\text{cm}$	$10.51\mu\text{m}$	$0.347 \Omega/\text{sq}$
$L=2\text{cm}, b=1.2\text{cm}$	$10.12 \mu\text{m}$	$0.337 \Omega/\text{sq}$

The Alpha Step IQ (nanoFAB, at the University of Alberta) is used to measure thickness for these lines of ink,  $d = 10\mu\text{m}$  is measured in average after two times measurement. The four point probe provides the sheet resistance as  $R_s = 0.347 \Omega/\text{square}$ . Then, the bulk (volume) resistivity can be calculated as  $\rho = 0.347 \times 10\mu\text{m} = 3.47 \times 10^{-4} \text{ohms} - \text{cm}$ . This resistivity is equivalent to the conductivity of  $2.8751 \times 10^5 \text{s/m}$ .

Table 4-2: The resistivity, sheet resistance for silver ink, and the resistivity of copper. The conductivity of copper is  $5.96 \times 10^7 \text{S/m}$ .

Bulk Resistivity ( $\rho$ )	Sheet Resistance ( $R_s$ )	Resistivity (Copper)
$\Omega\text{-m}$	$\Omega/\text{square}$	$\Omega\text{-m}$
$3.47 \times 10^{-6}$	$0.347 \Omega/\text{square}$	$1.59 \times 10^{-8}$

This value is incorporated in HFSS design in order to design two MTL resonators with conductive ink as conductive material. Finally, two resonator (PLA

and ABS) substrates are 3D printed and conductive ink is printed on them using the customized 3D printer. The individual parts are printed as shown in Figure 4-5. Then, the parts are attached to each other by snapping and some amount of glue can be used for improved adhesion. For more details about ink printing process see appendix 0.

## 4.2 Fabrication Challenges

**Adhesion between first layer and heat-bed:** There must be enough homogenous heating for the first layer in order to adhere to the print bed. There are heaters located under the print bed that provide heat for print bed. The heating process must be homogenous in order to provide adequate adhesion for first layer because this layer is the fundamental part of structure. Also, print bed surface must provide good adhesion for plastics. If these conditions are met, the printed layer will not come off while printing other layers.

**Material bonding:** Gap between layers happen when layers do not get enough energy for bonding. A good curing mechanism can help layer bonding.

**Warping:** Warping was noticed mostly in PLA material. Warping is usually caused by temperature gradients in the material and different shrinkage of parts depending on the process. It can be attributed to the low mechanical strength of the printed layers or material bonding. Also air flow from environment can cause warping. An enclosed chamber can eliminate this issue.

**Soldering on ink:** Soldering to make electrical connection with outside world is impossible with this ink.

**Surface roughness:** Surface roughness is not a critical issue in the fabrication of MTL resonators. The amount of surface roughness is negligible and doesn't affect the MTL resonator's performance. Although, it has to be stated that a high surface

roughness can become a critical issue in the 3D-printed parallel plate capacitor sections of MTL resonators. If the parallel plate capacitor's surface has high roughness the capacitance will not match the designed model.

**Ink flow and clogging:** Ink flow from syringe should be constant to make uniform layers. A pressure on the dispenser setting must be adjusted to satisfy this condition. Ink flow depends on the syringe tip diameter. For nanoparticle inks, small tip sizes can be used but in this project a tip diameter of  $600\mu m$  is utilized. Ink being clogged inside syringe is an issue. In this project, initially, higher pressure is used to unclog the ink after long pause events.

### 4.3 Summary

3D printing as an advancing new manufacturing technology to build MTL coils is introduced in this chapter. The thermoplastic materials used to build RF coils are outlined first. Then a desktop 3D printer is customized to add ink printing capabilities. Ink resistivity and conductivity are measured using four point probe and are compared to copper. The printer modification process is described in detail. The modified 3D printer is used to print substrate for MTL coils, and it is used to print conductive ink on plastic substrates, rendering this technology for MRI coil design and fabrication applications.

## **Chapter 5 Design of MTL Resonators and Measurement**

Typically, RF microstrip coils are quasiplanar transmission lines with special lengths that correspond to the coil's resonant frequency. Microstrip coils are simple and efficient to use in higher MR frequencies [59]. RF coils are essential in magnetic resonance imaging (MRI) hardware for transmitting and receiving the resonant signal. In this chapter, the design aspects of MTL resonator, which can be used as single transceiver element in array, are demonstrated, and 3D printing is introduced as a new approach for low cost coil fabrication and labour free prototyping. In this thesis, state of the art design of parallel plate matching/tuning capacitors integrated to MTL resonator is outlined. MTL resonators made by ink or copper tape conductive layers are characterized based on their Q and SNR values. It is shown that 3D printing could provide the potential for developing semi air filled MRI coils.

### **5.1 MTL Resonator's Design Procedure**

The proposed MTL resonator is shown in Figure 5-1, which includes a semi air-filled substrate with monolithically-included capacitors. The resonator's electrical length is adjusted using capacitors on both sides. There are three vertical posts and two vertical walls attached to 13 cm microstrip line to hold it 1 cm above the ground plane. In Figure 5-1, "red" represents conductive layers and "green" layers represent the 3D printed substrate. From the design it can be seen that there is mostly air in between the ground plane and the microstrip line representing semi air-filled dielectric which reduces the dielectric loss in the resonator. In order to be able to implement the coil using 3D printer and satisfy the technological limitations (explained in Chapter 4), the resonator is printed in two sections: ground plane with holes for vertical posts and walls, and the signal line with capacitors and vertical posts. The process of printing resonators with ink is different than this process as explained in the section 4.1.1.

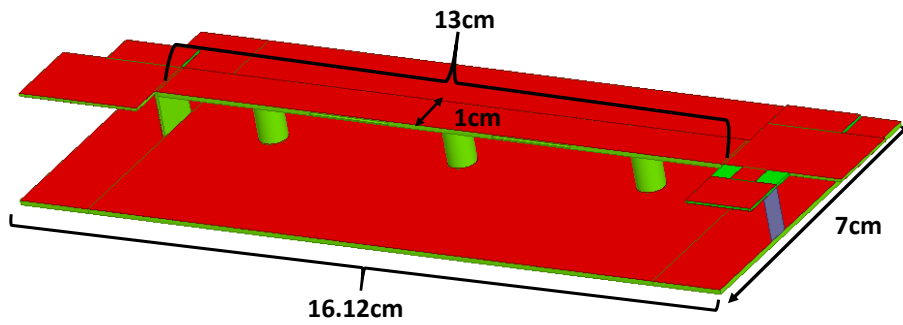


Figure 5-1: CAD drawing of the 3D printed partially air-filled microstrip coil with integrated capacitors

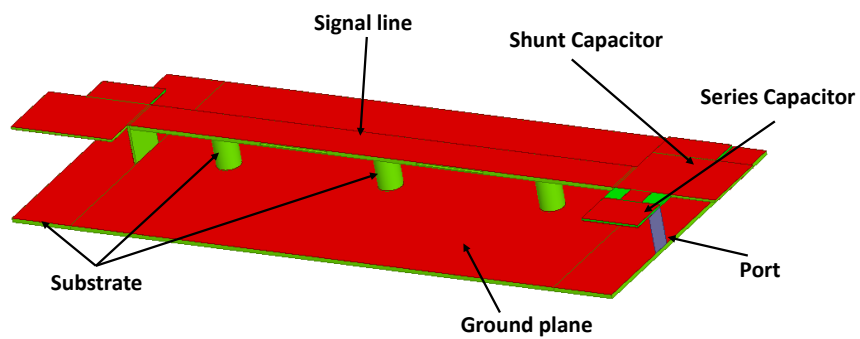


Figure 5-2: MTL resonator showing conductive layers (red) and substrate (green)

The ground plane is attached to a 0.1 cm thick substrate that is printed with holes to mount the signal line. In Figure 5-2, different sections of the MTL resonator is shown. Two shunt capacitors at both ends and one series capacitor is used for matching and tuning of the resonator for 4.7T scanner.

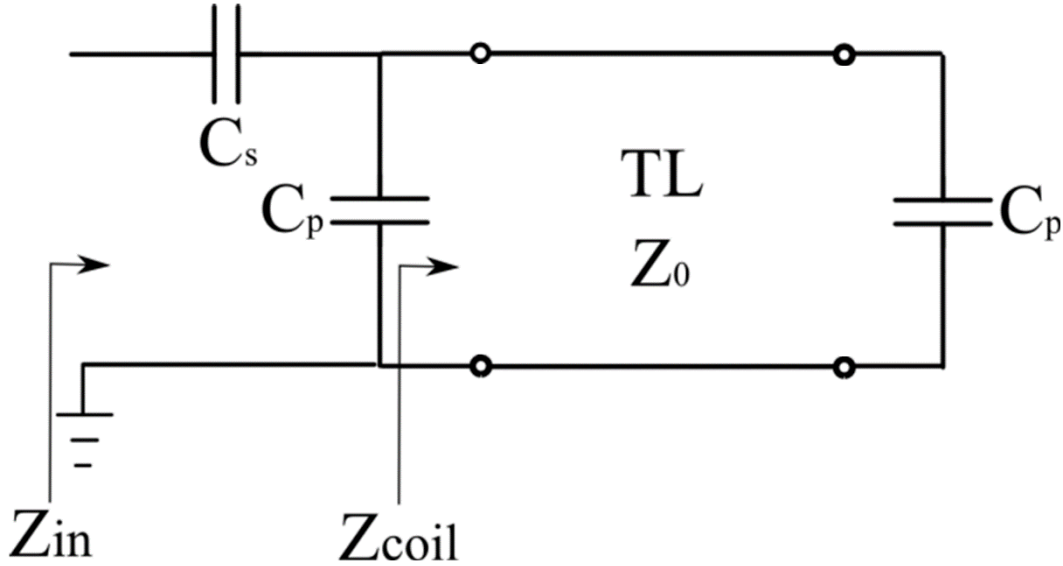


Figure 5-3: Circuit model of resonator with tuning and matching capacitors

In Figure 5-3, both shunt capacitors have the same capacitance value  $C_p$  where the top plate is connected to the signal line and the bottom plate is connected to the ground. Parallel plate capacitors are designed for shunt and series capacitors and the 3D printed thermoplastic materials are used as dielectric between plates.  $C_s$ , the series capacitor, is connected to the coaxial port on one side and to the signal line from the other.

In Figure 5-2, the ground plane is laid on the substrate instead of being on the bottom of substrate. This approach follows the idea of inverted MTLs presented in [59]. Therefore, dielectric loss is reduced by reducing the amount of dielectric in the area between signal line and ground. The signal line is separated from the ground plane with 3 vertical cylinders spaced 4.35 cm apart. The gap between the strip and ground plane is 1cm, which is mostly air. The input impedance of the coil that is shown in the circuit model shown in Figure 5-3, is given by:

$$Z_{coil} = Z_0 \frac{\frac{1}{j\omega C_p} + jZ_0 \tan \beta l}{Z_0 + j \frac{1}{j\omega C_p} \tan \beta l}, \quad (5-1)$$

where  $Z_0$  is the characteristic impedance of the transmission line,  $\beta$  is the propagation constant, and  $l$  is the line length (13cm). The input impedance of the

resonator  $Z_{in}$  has to be matched to  $50\Omega$  for optimal preamplifier noise factor matching for receiving and maximum power transfer in transmission. Ansoft HFSS for simulation, and Agilent ADS to analyze the matching and tuning conditions are used in this thesis. In order to match this resonator to  $50\Omega$ , a two port resonator composed of microstrip transmission line and ground plane without end capacitors is simulated in HFSS with copper conductors, then the S-matrix is exported to ADS by using a circuit model shown in Figure 5-3. In HFSS simulation the permittivity of thermoplastic ABS or PLA is assumed to be 2 for initial simulation. Two square shape lumped ports are used to excite the structure in order to extract the S-parameters. Since four different materials (three thermoplastic material and one low loss foam material) are used to build the RF coil resonators in this thesis, the design provides the capability of re-tuning and re-matching at any point of measurement by means of modifying the parallel plate capacitors. The calculation of shunt and series capacitors are explained in [60]. The resonant frequency of circuit model in ADS is chosen 200MHz, and capacitors shown in Figure 5-3 are tuned as such to have  $Z_{in} = 50\Omega$ . This condition can be achieved by  $S_{11} < -30dB$  at the port.

The shunt capacitor on the microstrip end is chosen as such that it is equal to the shunt capacitor at the input in order to electrically balance the resonator. MTL coils that are designed here are 3D printed using the 3D printers described in Chapter 4. Various MTL coils are fabricated with ink or copper as conductive material and their performance will be compared to standard MTL coil with foam dielectric. The parallel plate capacitors model introduced in this chapter eliminates the need for high cost variable/fixed capacitors, and fastens the fabrication process.

### 5.1.1 Permittivity and Loss Tangent Extraction

The effective permittivity of a mixture is given by [61], and it can be shown for mixture of plastic and air:

$$\varepsilon_{eff} = \varepsilon_{plastic}^f \times \varepsilon^{(1-f)}_{air} \quad (5-2)$$

where  $\varepsilon_{eff}$  and  $f$  are the effective permittivity and volume fraction of the mixture [61]. The volume fraction for mixture of two materials is:

$$f = \frac{(v_{plastic})}{(v_{plastic} + v_{air})} \quad (5-3)$$

as it can be seen from this equation, when the volume fraction is reduced, the effective permittivity reduces. In design of the MTL resonators in this thesis, the mixture of plastic and air contribute to the bulk permittivity and as much the air is increased (section 5.1.2), the bulk permittivity changes. The dielectric constant of PLA trace is close to 3 [62], [56], and the volume fraction can be calculated from effective permittivity.

In order to find the bulk substrate permittivity of these partially air-filled structures, HFSS simulation and physical bench-top measurements are used. First an initial design is done and then the prototypes are printed and evaluated. The details are explained below.

Since fabrication variations can change these parameters, the MTL resonator is designed at first, based on the initial assumptions for these parameters ( $\epsilon_r = 2$  and  $\tan\delta=0.02$ ) and the capacitor values are extracted from ADS. The S-parameters are extracted and fed into the ADS circuit model and capacitor values are driven to matching at 200MHz. The advantage of this method is that any iteration of the dielectric constant can be found from measurement data. From the values that the ADS simulation result provided, shunt and series capacitors at both sides are designed as shown in Figure 5-2. A copper thickness of  $t_c = 32\mu m$  has been used to represent the copper tape. The final capacitance dimensions are used in the 3D printable model. The desktop 3D printer (X-series, Machina Corp) uses Slic3r software to generate g-code from a .stl file.

The resonator is printed in two sections (microstrip line with capacitors and posts, and the ground plane). Then, the conductive tape is attached for signal line, capacitor plates and ground plane. The necessary connections are made with soldering. The coaxial SMA connector is soldered to excite the resonator from one port as it is seen in Figure 5-2. The port is defined between bottom plate of the series capacitor (the decoupling capacitor) and ground plane as it can be seen in

Figure 5-3.

Measurements are performed on a  $36 \times 26 \times 11 \text{ cm}^3$  phantom filled with  $3.6 \text{ g/l}$  NaCl and  $1.96 \text{ g/l}$   $\text{CuSO}_4 \cdot 5\text{H}_2\text{O}$  to emulate the human body ( $\epsilon_r=76$ ,  $\sigma=0.8 \text{ S/m}$ ). In HFSS simulation, a box with the same size and electrical properties are used. Measurements of  $S_{11}$  were performed on a Rohde & Schwarz ZVL3 vector network analyzer following a Short-Open-Load-Thru (SOLT) calibration to account for cable losses and phase shifts [63], [64].

Since an initial pre-assumed dielectric constant and loss tangent were used in HFSS simulation, the resonant frequency in bench-top measurement was 20MHz off-resonance. Therefore, in the next step, the permittivity of substrate and loss tangent is tuned to match the same frequency. The permittivity and loss tangent of each resonator is tuned to match the measured results in terms on resonance frequency and quality factor. Finally, the values for dielectric constant and loss tangent for thermoplastic materials are extracted. The complex permittivity for PLA, ABS and UV-resin are estimated from measurement results and are listed in Table 5-1. As well the volume fraction values are extracted from equations (5-2), and (5-3) based on the measured complex permittivity and reported permittivity values for each plastic:

Table 5-1: Complex permittivity for plastics used for RF coils

<i>Material Name</i>	<i>Complex Permittivity</i>	<i>Volume Fraction (f)</i>	<i>Permittivity Reported</i>
PLA	$1.24(1+i \cdot 0.005)$	0.19	3 [62], [56]
ABS	$1.34(1+i \cdot 0.008)$	0.27	2.87
UV-resin	$2.0(1+i \cdot 0.026)$	0.46	4.5 [65]

### 5.1.2 Substrate Design for Reduced Loss, Semi Air-filled Dielectric

An advantage of 3D printing is that it allows early design iteration to reduce the amount of dielectric in MTL coil's structure. Considering the fact that the thermoplastic materials (ABS, PLA, UV-curable resin) that are used for the MTL design have considerable loss tangent, in order to develop high quality factor 3D printed coils, few modifications have been done. One main technique is to remove the substrate under the microstrip line to create air type substrate. However, the

structure should still hold mechanically, therefore, three hollow posts (similar to the ones shown in Figure 5-4) are utilized. In addition, an inverted ground plane is utilized, meaning that the conductive material is located on top of the supporting thermoplastic material as shown in the Figure 5-4.

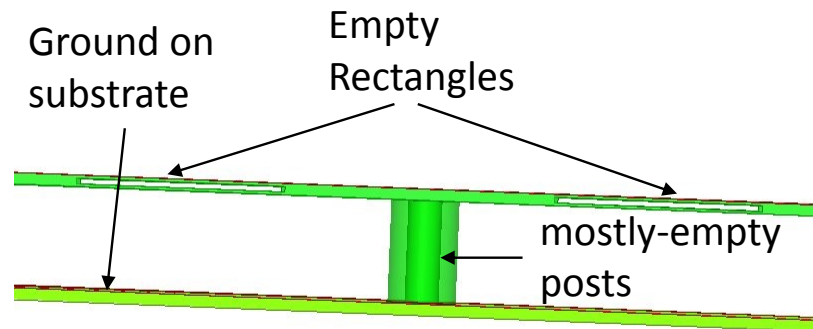


Figure 5-4: substrate-free areas are introduced into design to reduce the dielectric loading effects on MTL resonator performance.

High resolution 3D printer can fabricate precise cavity geometries, and that capability empowers the design of MTL resonators.

## 5.2 Coil Simulation and Results

Quality factor is an essential value of any resonant circuit as well as RF coils. It will be frequently used to determine the performance of RF coil [66], [67]. Increasing the Q of the coil the signal to noise ratio (SNR) will be enhanced. The Q for RF coils is usually measured as loaded (with sample) and unloaded (on the bench). The input signal matching condition is achieved only in loaded condition. Q for a resonator is defined as frequency of resonance divided to relative 3dB bandwidth.

The  $Q_{unloaded}$  values are measured and matched with simulation to extract the loss tangent values for each material. With this method, the required  $C_p$  and  $C_s$  is predicted to be 19.51pF and 3.84pF, respectively. To realize these capacitors, parallel plate approximation is considered. Using a spacing of 0.1cm between the parallel plates, the required capacitors are designed to match the MTL resonator to

200MHz.

The dimensions of final shunt and series capacitors for different thermoplastic materials used in this thesis are listed in

Table 5-2 - Table 5-4. The values that are provided in these tables are for PLA, ABS and UV-curable resin material with copper tape as conductive line.

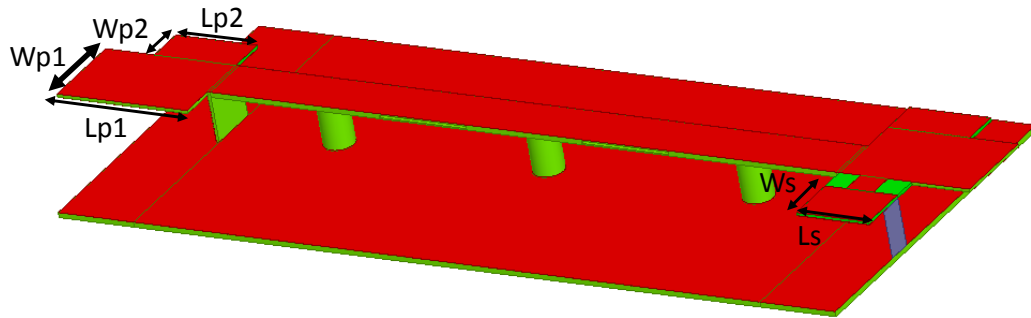


Figure 5-5: Final capacitor dimensions for MTL resonator

Table 5-2: The MTL resonator capacitor dimensions for PLA plastic

Capacitor	Width (cm)	Length (cm)
Shunt Capacitor $C_p$	$W_{p1}=2.9, W_{p2}=1.1$	$L_{p2}=1.9, L_{p1}=2.7$
Series Capacitor $C_s$	$W_s=1.5$	$L_s=1.5$

Table 5-3: The MTL resonator capacitor dimensions for ABS plastic

Capacitor	Width (cm)	Length (cm)
Shunt Capacitor $C_p$	$W_{p1}=2.9, W_{p2}=1.1$	$L_{p2}=1.9, L_{p1}=2.56$
Series Capacitor $C_s$	$W_s=1.5$	$L_s=1.5$

Table 5-4: The MTL resonator capacitor dimensions for UV-resin plastic

Capacitor	Width (cm)	Length (cm)
Shunt Capacitor $C_p$	$W_{p1}=1.7, W_{p2}=0.75$	$L_{p2}=1.69, L_{p1}=2.7$
Series Capacitor $C_s$	$W_s=1$	$L_s=1.5$

In Figure 5-6, the simulated matching  $S_{11}$  (dB) for three resonators is shown. The matching condition measurement was previously introduced in [30], [32]. The substrate material's characteristics used to produce these results are based on the substrate analysis results obtain in section 5.1.1. As it can be seen in Figure 5-6, the matching condition for ABS and PLA plastics is similar, that can be attributed to their similar dielectric constant. The simulated  $S_{11}$ (dB) of UV-resin is around -19.5dB. Better matching conditions for this resonator can be achieved by varying the series capacitor dimensions shown in Figure 5-2, and Table 5-4. In this way, the inductance seen from the port is changed. Smith chart analysis is the recommended approach to find matching condition [68]. In fact this approach has been used here and is explained in the next section.

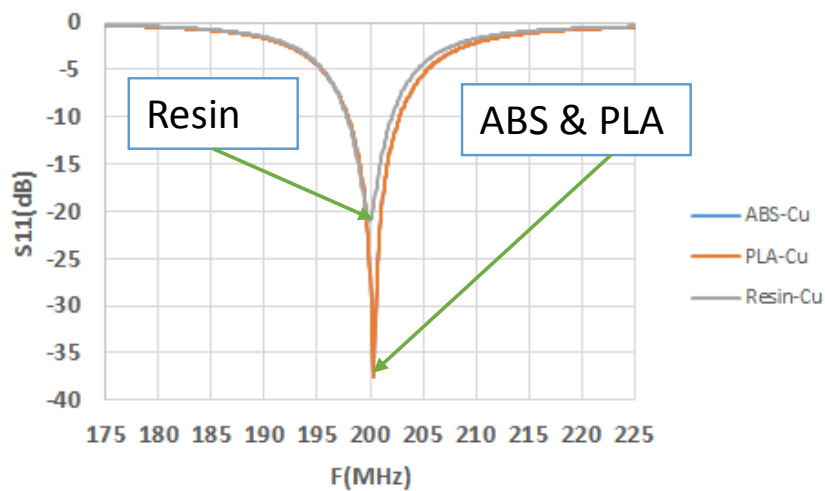


Figure 5-6: The  $S_{11}$  (dB) simulated results showing match at 200MHz for three resonators

## 5.2.1 Matching Improvement

In resonator design in [68], [30] the measured  $S_{11}$ (dB) matching value is -40dB, although with a value less than -10 dB, an acceptable performance can be achieved. If the condition of matching is higher than -10dB, a higher RF power is needed from power amplifier so the transmit efficiency will be degraded. Therefore a good care should be taken for precise matching condition in coils. Here, the Smith chart is used to demonstrate the matching condition.

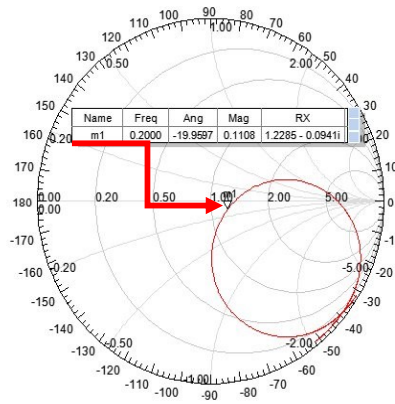


Figure 5-7: Smith chart model, resonance frequency matching at 200MHz for UV-resin resonator

The MTL resonator shown in Figure 5-5 should be matched. The input impedance of this resonator must be matched to  $50 \Omega$  of coaxial cable. Therefore, in order to investigate the input impedance at port 1,  $S_{11}$  is shown in smith chart. As it can be seen in Smith chart for marker m1 at 200 MHz, the impedance seen is  $R_x = 1.2 - i0.0941$ . It has to be noted that real part of input impedance should be 1 and imaginary part should be close to zero in order to find a good match. It has to be stated that the amount of RF power required for transmit is reduced with better return loss. In order to find good matching, an optimization is done to the series capacitance width  $W_s$ , which requires decreasing or increasing dimension of the series capacitor to find a better match.

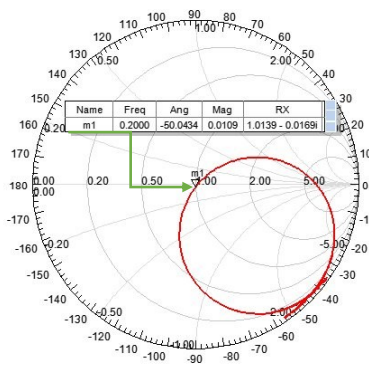


Figure 5-8: Smith chart model, resonance frequency matching after iterations at 200MHz for UV-resin resonator.

In Figure 5-8, it can be seen that a better matching at point  $R_x = 1.0139 - 0.0169$  on the smith chart, corresponding to  $S_{11} = -35\text{dB}$ , is achieved by making small increment to series capacitance width  $W_s$ . It has to be noted that by changing the width of series capacitance, the  $S_{11}$  at 200 MHz should get real part 1 and the imaginary part (inductive or capacitive) close to zero. By doing so, the input impedance close to  $50 \Omega$  is achieved.

### 5.3 Printed MRI Coils Realization

To have a full scale study of the MTL coils, 8 different MTL coils are fabricated as listed in Table 5-5 that includes various polymers in combination with copper tape and conductive ink. In addition, a traditional MTL resonator of similar dimensions was built for comparison using low-loss Rohacell foam (Evonik Ind.) [69] substrate, copper tape conductors, fixed porcelain capacitors (American Technical Ceramics), and trimmer/variable capacitors (Murata Electronics North America). The trimmer/variable capacitors were also used in the resonators 1, and 3 to match them to 200 MHz.

Table 5-5: The resonators type and built capacitors types

<i>Resonator</i>	<i>Design-Type</i>
1	PLA with commercial fixed/variable capacitors
2	foam with commercial variable capacitors
3	ABS with commercial fixed/variable capacitors
4	ABS with built-in 3D printed capacitors
5	UV-resin with built-in 3D printed capacitors
6	PLA with built-in 3D printed capacitors
7	ABS with built-in 3D printed capacitors – ink printed
8	PLA with built-in 3D printed capacitors – ink printed

To make connections for MTL resonators with copper as conductive layer, one SMA connector is soldered between bottom plate of series capacitor and ground plane. In order to make electrical connections to MTL resonators with ink layer, soldering on the ink is difficult since ink is sensitive to soldering temperature. As a solution, a small piece of copper tape is used on the substrate and connections are made between two pieces of copper tape on bottom plate and ground plane. Then ink is used to connect this to the rest of the capacitor plate (in this way, soldering on ink is eliminated). Another possible way is to use a conductive paste for electrical connections, but since it has very high electrical resistivity it degrades the coil's performance.

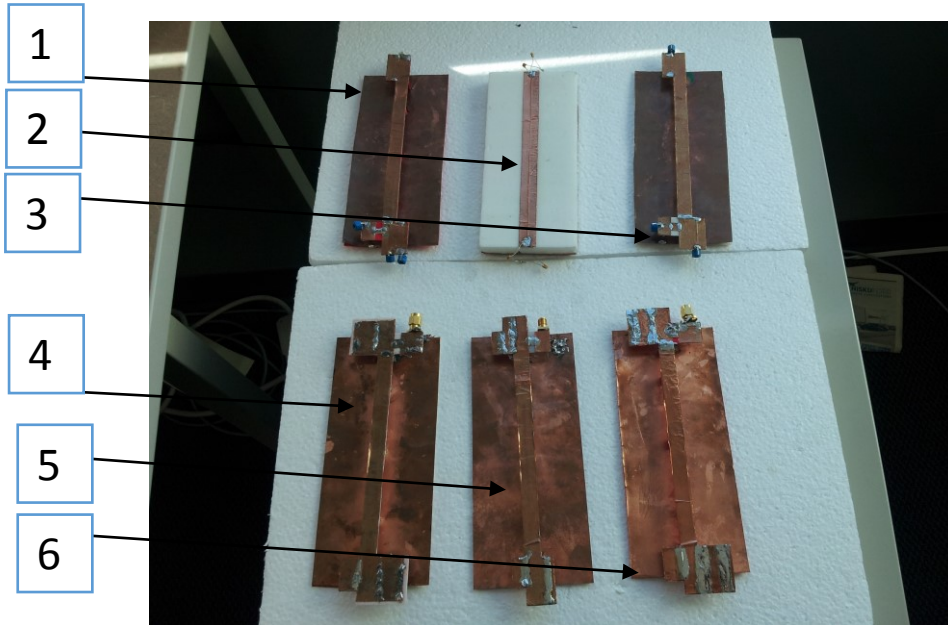


Figure 5-9: Fabricated resonators with copper: (1,3) PLA and ABS with commercial tuning capacitors, respectively. (2) Standard resonator with low loss Rohacell foam, (4,5,6) ABS, Resin, PLA resonators with built-in parallel plate 3D printed capacitors.



Figure 5-10: (7) ABS with ink, (8) PLA with ink.

In Table 5-5, MTL resonators 1 and 3 were designed before knowing the exact permittivity for PLA and ABS, and the external tunable capacitors were used to tune them to 200MHz. Then, the resonators without commercial capacitors (4,5,6,7,8) were built.

Figure 5-11 shows the simulation results based on the characterized substrate and ink, and the fabrication constraints are explained in this chapter. The 3D printer provides the capability of prototyping custom-designed MTL resonators with a variety of designs eliminating the need for external capacitors. As it is shown in Figure 5-9, resonators 4,5,6 are designed after the permittivity and loss tangent is tracked from MTL resonators (1,3). Also, resonators (4,5,6) with 3D printed parallel plate capacitors (3D printed plastic and copper tape) are matched and tuned to 200MHz. The final resonators printed with ink are shown in Figure 5-11. As it can be seen, the S11 (dB) for both resonators is less than -30dB and that proves high matching condition for these resonators.

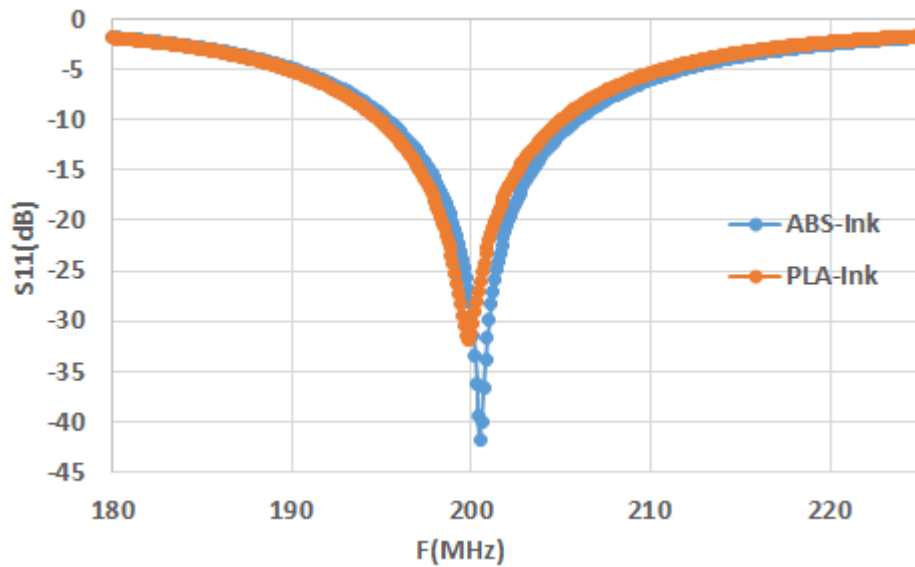


Figure 5-11: S11(dB) loaded-matching in simulation results showing two 3D-printed ABS and PLA resonators with silver ink as conductive layer.

## 5.4 Bench Measurement Setup and Return Loss Results

In this chapter, various MTL resonators with different substrates were fabricated. The 3D printing as a new approach to fabrication of MRI coils was introduced in Chapter 4. In this section, the measurement process for the fabricated resonators to match them to the Larmor frequency of 200 MHz is described. Once the design is complete the 3D printed resonators with copper tape or conductive silver ink are prepared for bench measurement. As it was discussed in section 5.2, the measurement and simulation for matching, is done in the presence of a phantom.

Measurements are performed on a  $36 \times 26 \times 11$  cm<sup>3</sup> phantom, filled with 3.6 g/l NaCl and 1.96 g/l CuSO<sub>4</sub>·5H<sub>2</sub>O, to emulate the human body ( $\epsilon_r=76$ ,  $\sigma=0.8$  S/m). In simulation, a box with the same size and electrical properties are used. Measurements of S<sub>11</sub> were performed on a Rohde & Schwarz ZVL3 vector network analyzer following a Short-Open-Load-Thru (SOLT) calibration to account for cable losses and phase shifts. One port S<sub>11</sub> measurement is conducted for each resonator on the phantom. The precise Larmor frequency of 4.7T is 200.4MHz so all resonators are tuned and matched to that frequency precisely with some iterations on the capacitor's lengths and widths. It has to be stated here that 1cm distance (phantom plastic and foam) is maintained between resonators and phantom surface.

In Figure 5-12, the loaded measurement for S<sub>11</sub> (dB) is shown. All six resonators are placed at the position shown and their matching data is recorded and compared with HFSS simulation.

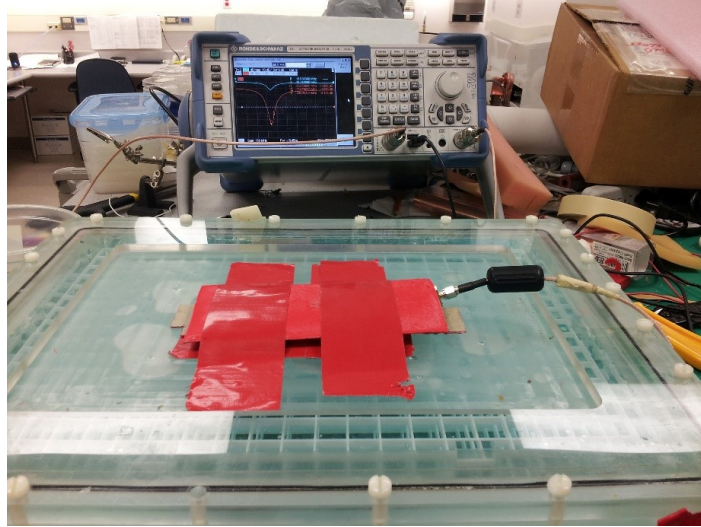


Figure 5-12: loaded matching bench measurement set-up, matching resonators to 200.4MHz for 4.7T MRI system.

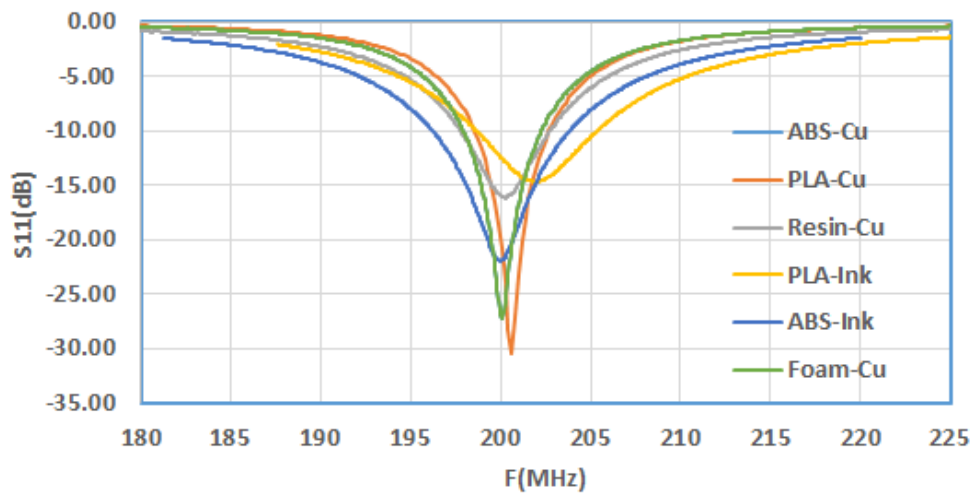


Figure 5-13: Matching S11 (dB) loaded measurement results.

In Figure 5-13, measurement results shows that for ABS, PLA, foam resonators with copper conductors,  $S_{11} < -25\text{dB}$ ; for UV-curable resin,  $S_{11} = -15\text{dB}$ ; and for ABS-ink  $S_{11} = -22\text{dB}$ . For PLA-Ink the matching is slightly off the resonance, but selecting a marker at 200.4MHz the correspondent matching value is  $S_{11} (\text{dB}) = -12\text{dB}$ . It has to be noted that small iterations can be done for PLA-Ink resonator to match this resonator to 200MHz. The current values of matching would be adequate for taking MRI images.

## 5.5 MR Measurement Results and Discussion

Loaded and unloaded  $Q$  of each resonator is measured according to [45] using a network analyzer. Gradient-echo imaging ( $T_R/T_E = 50/5$  ms, flip angle =  $10^\circ$ , bandwidth = 391 Hz/pixel, acquisition matrix  $256 \times 128$ , FOV =  $30 \times 30$  cm, 1 average) is performed on a 4.7 T Varian system to compare signal to noise (SNR) performance.

All six MTL resonators that were fabricated and matched/tuned to 4.7T Larmor frequency, 200MHz, are placed in loaded and unloaded conditions as previously discussed and their  $Q$  values are calculated. The loading factor values are extracted from  $Q$  data and are demonstrated for six coils in Table 5-6. The efficiency values of 3D-printed coils with copper lines are very similar to low loss standard foam resonator, this proves the fact that 3D printing can be adopted as a new fabrication technology to custom-design MRI coils. Matching,  $Q$ -factor, efficiency ( $\eta = 1 - Q_l/Q_u$ ) [70], and average SNR in three sagittal slices (one central and two offset  $\pm 1.5$ cm;  $13 \times 4$  cm<sup>2</sup> area) of the six resonators are compared in the Table 5-6.

Table 5-6: Measurement values for  $Q$  factor, Loading factor ( $\eta$ ), and SNR for six coils.

RF Coil Construction	Matching $S_{11}$	$Q_{\text{unloaded}}$	$Q_{\text{loaded}}$	Efficiency $\eta$	Image SNR
<i>PLA+Cu</i>	-30dB	98.9	29.8	0.69	41.5
<i>ABS+Cu</i>	-30dB	79.3	33.1	0.58	59.4
<i>Resin+Cu</i>	-15dB	40.4	28.07	0.30	40.5
<i>PLA+ink</i>	-22dB	29	18.2	0.37	29.4
<i>ABS+ink</i>	-22dB	28.5	22.6	0.20	53.1
<i>Foam+Cu</i>	-30dB	122.8	51.4	0.58	42.4

The efficiency values of 3D-printed resonators with ink and UV-resin with copper are less than a standard foam resonator. Resonators made with PLA and

ABS show comparable  $Q$  and efficiency to those resonators made with Rohacell, while the losses in UV-curable resin are much worse. Even though silver ink is more lossy than copper due to its lower conductivity ( $2.9 \times 10^5$  S/m compared to  $5.9 \times 10^7$  S/m), the consequent reduction in image SNR is very limited. An alternative ink with higher conductivity has already been found (PChem, PFI-722 silver nanoparticle ink,  $1.9 \times 10^7$  S/m) that will provide  $Q$  performance nearly equal that of copper. The SNR values are the average signal to noise ratio from three sagittal slices.

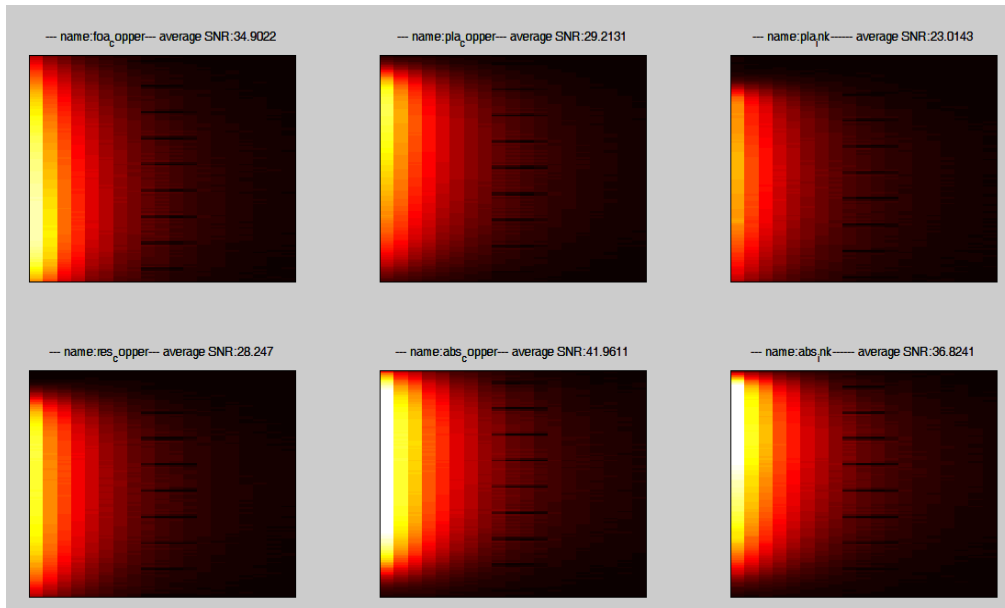


Figure 5-14: Sagittal slice 1 and the SNR for six different coils are shown.

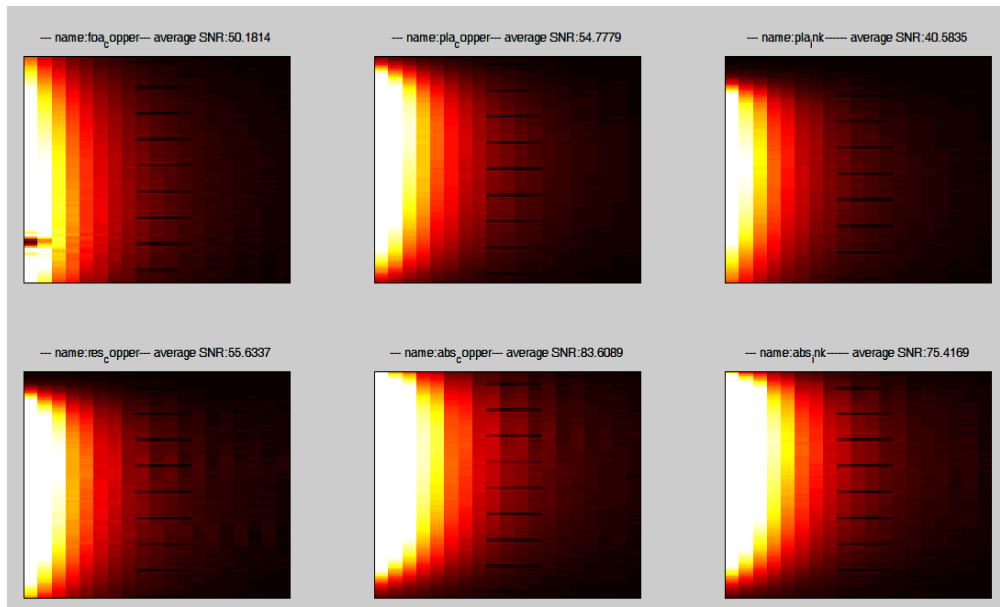


Figure 5-15: Sagittal slice 2 and the SNR for six different coils are shown.

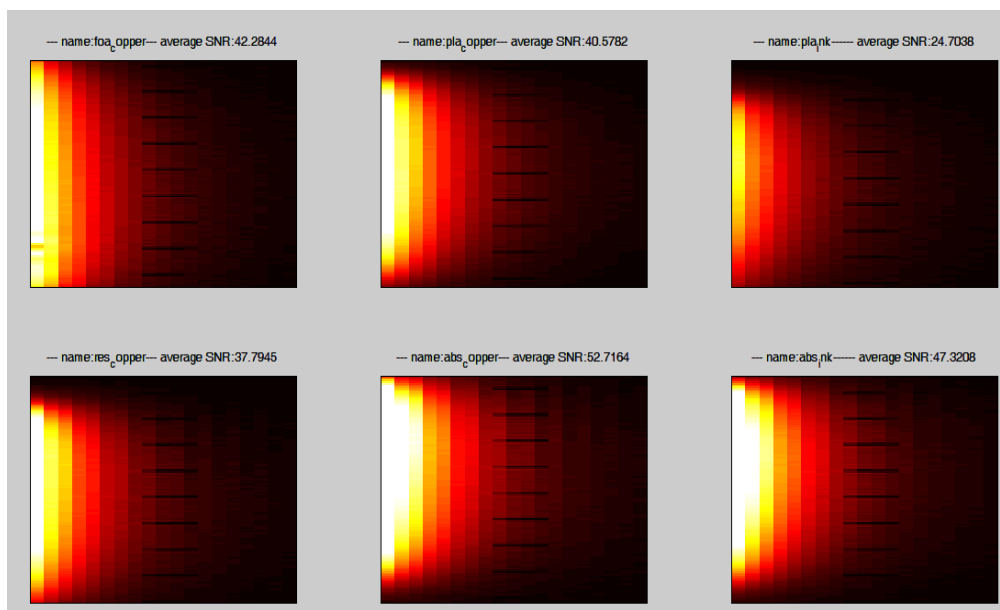


Figure 5-16: Sagittal slice 3 and the SNR for six different coils are shown.

The SNR values are calculated by averaging these three slices for each coil and represented in Table 5-6. The black dot shown in sagittal 2 at foam-Cu resonator is a bubble that were present inside the phantom. The fact that the SNR results are close, regardless of conductor type, can be accounted for by the noise factor from RF amplifier and coaxial transmission line, which dominates the

equivalent resistance of the coils. A coronal and one sagittal image of each six resonator's  $B_1$  profile in the field of view are shown below.

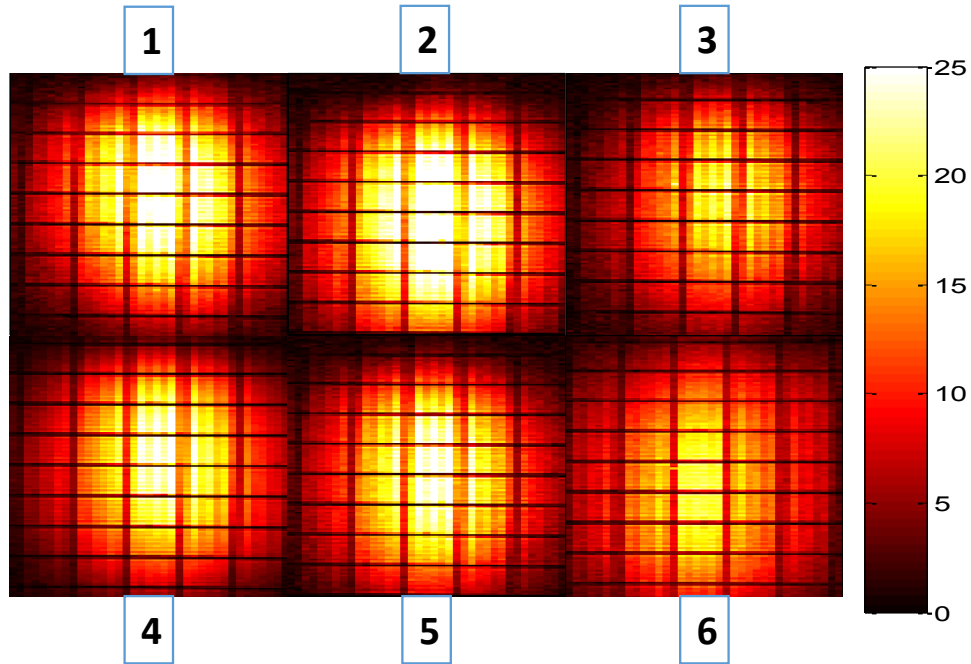


Figure 5-17: Coronal image of six resonators with SNR bar. Numbers correspond to type of resonators in Table 5-7. This image is driven from  $8 \times 15$ cm of the field of view.

The slice is selected at the center of the sample. As it can be seen from the SNR bars, the value from sagittal images are higher and that is because sagittal slice is in parallel to the transmit field direction. In Table 5-7, the SNR values for MTL coils corresponding to numbers in Figure 5-17 and Figure 5-18 are listed.

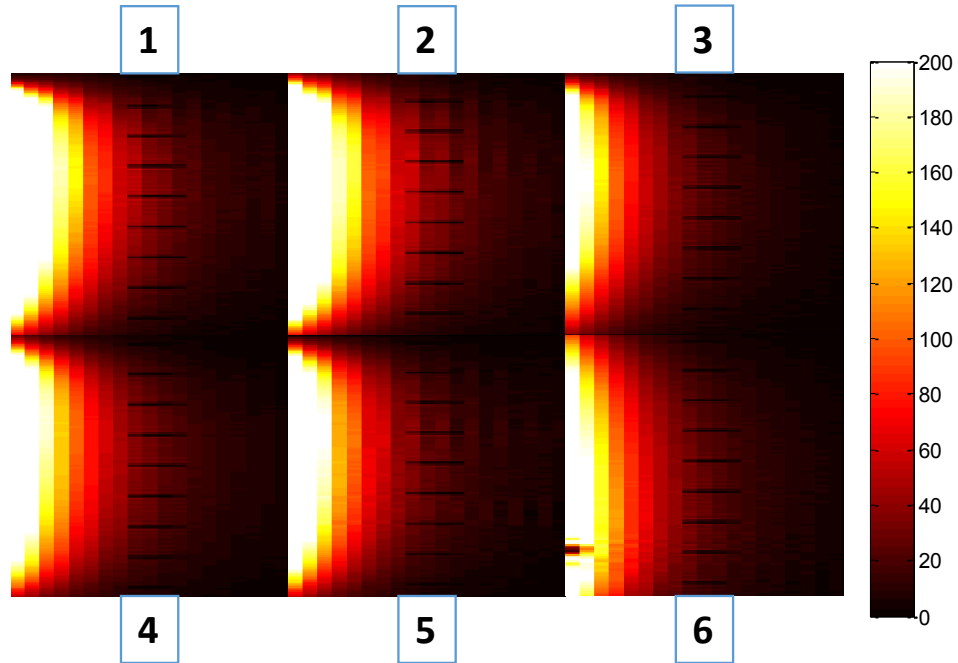


Figure 5-18: Sagittal image of six resonators with their SNR bar. Numbers correspond to the type of resonators as shown in Table 5-7.

Table 5-7: Calculated SNR values for Sagittal and coronal slices

Number	Resonator	SNR	SNR
		Coronal	Sagittal
1	<i>ABS+ink</i>	9.75	75.39
2	<i>ABS+Cu</i>	10.94	84.03
3	<i>PLA+ink</i>	7.05	41.56
4	<i>PLA+Cu</i>	8.68	54.74
5	<i>Resin+Cu</i>	8.83	56.23
6	<i>Foam+Cu</i>	8.43	50.15

Resin has higher loss tangent and low efficiency is expected. SNR value for resin doesn't match with the expectation of efficiency. The efficiency is measured on the bench. SNR is measured inside the scanner and there are other factors that SNR value can be affected by, such as: flip angle. In Table 5-7, coronal and sagittal SNR values for six coils are listed.

## 5.6 Summary

In this chapter, the design aspects of MTL resonator for 4.7T MRI system are described. MTL resonators with built-in capacitors were used to determine the complex permittivity of thermoplastic materials at 200MHz, and by knowing the permittivity and loss tangent values, MTL resonators were designed and fabricated with 3D printer.

In summary to this part, by knowing the permittivity of a 3D printing material a custom designed MTL coil can be printed for MRI applications and copper tape or commercial conductive inks can be used to make a full resonator. Initially, the polymers used in 3D printers (PLA, ABS and Resin) are characterized for RF performance in 4.7T MRI. The modified desktop printer is used to print conductive ink on resonators. Based on the measured and characterized data, as well as fabrication constraints, 8 different MTL coils are designed. The characterization of such coils is demonstrated with SNR and efficiency values in a comparison table.

## **Chapter 6 Conclusion and Future Work**

### **6.1 Summary and Conclusion**

This study shows the great potential and possibility of utilizing 3D printing technology to fabricate microstrip MR coils in an automated manner directly from 3D geometries used in simulations. Accurate characterization of the complex permittivity of the printed substrate is required in order to accurately simulate the coils and to reduce the iteration steps. Cost of MTL resonators fabrication is reduced significantly by adopting 3D printing technology. State of the art design and 3D printing of the parallel plate capacitors monolithically with MTL coil offers advantages in ease of fabrication, design iterations, and reduced time compared to standard MTL resonators. Multiple labour-intensive production steps such as soldering discrete capacitors in the traditional construction method are eliminated by accurate coil performance simulation and 3D manufacturing. Based on the achievements in this thesis a low cost 3D printer is customized to add ink printing capability. For the first time, the MTL coil's substrate and conductive layer is printed in one machine. MTL resonators are 3D printed using thermoplastics as carrier substrate and copper tape and silver inks for conductive layers. The printed MTL resonators are then measured and their performance is compared to a low loss foam MTL resonator.

Based on findings of this thesis, although there are variety of thermoplastic materials used in 3D printing technology, such as Resin, ABS and PLA, not all of them are suitable for RF devices. Among the ones studied in this work, ABS and PLA are superior and promising for MRI applications. Nevertheless, an important approach in MTL resonator design is to reduce the amount of dielectric used in the resonator which improves the coil performance since the dielectric loss, though small, is reduced. In addition, 3D-printed parallel plate capacitors can be used for matching/tuning the MTL resonators, and hybrid integration and soldering of variable capacitors for MTL resonators is eliminated.

Quality factor and SNR results shown in Table 5-6 demonstrate that 3D-printed MTL resonators have comparable performance to standard low loss foam

MTL resonators. ABS and PLA resonators with copper tape have shown high efficiency and SNR values. UV-curable resin with copper tape has lower efficiency compared to ABS and PLA, but it has similar SNR value. The efficiency and SNR values of resonators with ink are less than standard foam resonator. Even though silver ink is more lossy than copper due to its lower conductivity ( $2.9 \times 10^5$  S/m compared to  $5.9 \times 10^7$  S/m), the consequent reduction in image SNR is very limited.

Therefore, 3D printing technology can be used to fabricate MR compatible coils with reduced fabrication process steps. It has been shown that taking advantage of 3D model, variations in design leads to better performance in MRI.

## 6.2 Future Study

The research can be continued and further advanced by considering the following future works:

- Although, the SNR results demonstrate the conductive ink used in this measurement has comparable results to resonators with copper conductors, nanoparticle ink can be used as highly conductive material instead of our silver-ink to achieve higher efficiency and better SNR.
- The ink-printing process in our printer is limited to 2D orientations, but a printing nozzle with flexible springs can add the option of printing ink on 3D surfaces as well.
- New 3D printing plastic materials with better RF performance and mechanical properties can be used to make MR compatible coils.
- MTL resonator design can be modified to enhance the coil efficiency, and an array form of MTL resonators can be built to increase the SNR.
- Since parallel plate capacitors can replace conventional matching/tuning capacitors to lower cost and reduce labour work, further studies in the direction of designing and fabricating voltage variable 3D parallel plate capacitors can be beneficial. More importantly, the new material with low spring constant and high

accuracy can be used in 3D printing to facilitate the actuation of these capacitors.

### **6.3 MTL Resonators Fabrication Recommendations**

In order to reduce the amount of iterations in parallel plate capacitor's dimensions during measurement, a precise characterization of permittivity and loss tangent is required in advance. That can be done using a dielectric measurement setup. The rule of thumb is that, always, the dimensions of capacitors can be made slightly higher than the exact values, so they can be trimmed afterwards.

Parts with ABS material have shown good accuracy compared to PLA, and high resistance against ink solidification. The PLA material, after fabrication, has some gaps in between layers through which ink will sink, therefore the infill density in Slic3r can be increased to reduce the gaps, though it will degrade the coil performance in terms of efficiency.

If other material with higher melting points can be 3D printed for the substrate, then nanoparticle inks can be used and cured in an oven to gain better SNR and efficiency.

## References

- [1] M. Elmaoğlu and A. Çelik, *MRI Handbook*. NY, USA: Springer Science+Business Media, LLC, 2012.
- [2] Z.-P. Liang and P. C. Lauterbur, *Principles of Magnetic Resonance Imaging: A Signal Processing Perspective*. Wiley-IEEE Press, 2000.
- [3] D. Sappey-Marinier and A. Briguet, “Magnetic Resonance Imaging,” in *Medical Imaging Based on Magnetic Fields and Ultrasounds*, H. Fanet, Ed. John Wiley & Sons, Inc., 2014, pp. 73–262.
- [4] A. M. Maunder, “Strategies for Maximizing Signal to Noise in Decoupled Receive Coil Arrays for Magnetic Resonance Imaging,” Thesis, University of Alberta, 2013.
- [5] T. S. Ibrahim, “Analytical approach to the MR signal,” *Magn. Reson. Med.*, vol. 54, no. 3, pp. 677–682, Sep. 2005.
- [6] J. Wang, “NMR Signal Intensity And Receive Sensitivity,” *Proc. Intl. Soc. Mag. Reson. Med.* 15, P. 321, 2007
- [7] D. I. Hoult, “The principle of reciprocity in signal strength calculations—A mathematical guide,” *Concepts Magn. Reson.*, vol. 12, no. 4, pp. 173–187, 2000.
- [8] E. Fukushima, “Radiofrequency Coils for NMR: A Peripatetic History of Their Twists and Turns,” in *eMagRes*, John Wiley & Sons, Ltd, 2007.
- [9] M. Markl and J. Leupold, “Gradient echo imaging,” *J. Magn. Reson. Imaging*, vol. 35, no. 6, pp. 1274–1289, Jun. 2012.
- [10] Edelstein WA, Schenck JF, Hart HR, Hardy CJ, Foster TH, and Bottomley PA, “SURface coil magnetic resonance imaging,” *JAMA*, vol. 253, no. 6, pp. 828–828, Feb. 1985.
- [11] D. I. Hoult, C. N. Chen, and V. J. Sank, “Quadrature detection in the laboratory frame,” *Magn. Reson. Med.*, vol. 1, no. 3, pp. 339–353, Sep. 1984.
- [12] A. J. E. Raaijmakers, O. Ipek, D. W. J. Klomp, C. Possanzini, P. R. Harvey, J. J. W. Lagendijk, and C. a. T. van den Berg, “Design of a radiative surface coil array element at 7 T: The single-side adapted dipole antenna,” *Magn. Reson. Med.*, vol. 66, no. 5, pp. 1488–1497, 2011.
- [13] C. E. Hayes, W. A. Edelstein, J. F. Schenck, O. M. Mueller, and M. Eash, “An efficient, highly homogeneous radiofrequency coil for whole-body NMR imaging at 1.5 T,” *J. Magn. Reson.* 1969, vol. 63, no. 3, pp. 622–628, Jul. 1985.
- [14] Y. Zhu, “Parallel excitation with an array of transmit coils,” *Magn. Reson. Med.*, vol. 51, no. 4, pp. 775–784, Apr. 2004.
- [15] P. B. Roemer, W. A. Edelstein, C. E. Hayes, S. P. Souza, and O. M. Mueller, “The NMR phased array,” *Magn. Reson. Med.*, vol. 16, no. 2, pp. 192–225, 1990.
- [16] X. Zhang, Y. Liao, X.-H. Zhu, and W. Chen, “An MTL coil array with a broad frequency tuning range for ultra-high field human MR applications from 3T to 7T,” *Proc Intl Soc Mag Reson Med*, vol. 11, p. 1602, 2004.
- [17] D. O. Brunner, J. Paška, J. Froehlich, and K. P. Pruessmann, “Traveling-wave RF shimming and parallel MRI,” *Magn. Reson. Med.*, vol. 66, no. 1, pp. 290–300, 2011.

- [18] D. I. Hoult and D. Phil, "Sensitivity and power deposition in a high-field imaging experiment," *J. Magn. Reson. Imaging JMRI*, vol. 12, no. 1, pp. 46–67, Jul. 2000.
- [19] W. Mao, M. B. Smith, and C. M. Collins, "Exploring the limits of RF shimming for high-field MRI of the human head," *Magn. Reson. Med.*, vol. 56, no. 4, pp. 918–922, Oct. 2006.
- [20] J. T. Vaughan, H. P. Hetherington, J. O. Otu, J. W. Pan, and G. M. Pohost, "High frequency volume coils for clinical NMR imaging and spectroscopy," *Magn. Reson. Med.*, vol. 32, no. 2, pp. 206–218, Aug. 1994.
- [21] C.-P. Kao, Z. Cao, S. Oh, Y.-C. Ryu, and C. M. Collins, "Conventional volume coil and travelling-wave antenna for homogeneous excitation of the human head in MRI at 300 MHz," in *2010 IEEE Radio and Wireless Symposium (RWS)*, 2010, pp. 583–584.
- [22] N. D. Zanche, "Birdcage Volume Coil Design," in *eMagRes*, John Wiley & Sons, Ltd, 2007.
- [23] G. Giovannetti, R. Francesconi, L. Landini, M. F. Santarelli, V. Positano, V. Viti, and A. Benassi, "Conductor geometry and capacitor quality for performance optimization of low-frequency birdcage coils," *Concepts Magn. Reson. Part B Magn. Reson. Eng.*, vol. 20B, no. 1, pp. 9–16, Feb. 2004.
- [24] K. m. Gilbert, T. j. Scholl, and B. a. Chronik, "RF coil loading measurements between 1 and 50 MHz to guide field-cycled MRI system design," *Concepts Magn. Reson. Part B Magn. Reson. Eng.*, vol. 33B, no. 3, pp. 177–191, Aug. 2008.
- [25] D. I. Hoult and Paul C. Lauterbur, "The Sensitivity of the Zeugmatographic Experiment Involving Human Samples," *J. Magn. Reson.*, vol. 34, pp. 425–433, 1979.
- [26] G. Adriany, E. J. Auerbach, C. J. Snyder, A. Gözübüyük, S. Moeller, J. Ritter, P.-F. Van de Moortele, T. Vaughan, and K. Uğurbil, "A 32-channel lattice transmission line array for parallel transmit and receive MRI at 7 tesla," *Magn. Reson. Med.*, vol. 63, no. 6, pp. 1478–1485, Jun. 2010.
- [27] G. Adriany, P.-F. Van de Moortele, F. Wiesinger, S. Moeller, J. P. Strupp, P. Andersen, C. Snyder, X. Zhang, W. Chen, K. P. Pruessmann, P. Boesiger, T. Vaughan, and K. Uğurbil, "Transmit and receive transmission line arrays for 7 Tesla parallel imaging," *Magn. Reson. Med.*, vol. 53, no. 2, pp. 434–445, Feb. 2005.
- [28] X. Zhang, K. Ugurbil, and W. Chen, "Microstrip RF surface coil design for extremely high-field MRI and spectroscopy," *Magn. Reson. Med.*, vol. 46, no. 3, pp. 443–450, Sep. 2001.
- [29] S.-M. Sohn, L. DelaBarre, J. T. Vaughan, and A. Gopinath, "8-Channel RF head coil of MRI with automatic tuning and matching," in *Microwave Symposium Digest (IMS), 2013 IEEE MTT-S International*, 2013, pp. 1–3.
- [30] S.-M. Sohn, L. DelaBarre, J. T. Vaughan, and A. Gopinath, "8-Channel RF head coil of MRI with automatic tuning and matching," in *Microwave Symposium Digest (IMS), 2013 IEEE MTT-S International*, 2013, pp. 1–3.

- [31] H. A. Wheeler, "Transmission-Line Properties of a Strip on a Dielectric Sheet on a Plane," *IEEE Trans. Microw. Theory Tech.*, vol. 25, no. 8, pp. 631–647, Aug. 1977.
- [32] Y. Seo, "Design of microstrip-based surface coils for low-field small-bore MR applications," *Concepts Magn. Reson. Part B Magn. Reson. Eng.*, vol. 41B, no. 4, pp. 111–119, Oct. 2012.
- [33] P. Vernickel, P. Röschmann, C. Findekle, K.-M. Lüdeke, C. Leussler, J. Overweg, U. Katscher, I. Grässlin, and K. Schünemann, "Eight-channel transmit/receive body MRI coil at 3T," *Magn. Reson. Med.*, vol. 58, no. 2, pp. 381–389, Aug. 2007.
- [34] D. G. Gadian and F. N. H. Robinson, "Radiofrequency losses in NMR experiments on electrically conducting samples," *J. Magn. Reson. 1969*, vol. 34, no. 2, pp. 449–455, May 1979.
- [35] G. L. Pollack and D. R. Stump, "Electromagnetism," San Francisco, CA, Addison-Wesley, -620p, 2002.
- [36] C. Wang and G. X. Shen, "B1 field, SAR, and SNR comparisons for birdcage, TEM, and microstrip coils at 7T," *J. Magn. Reson. Imaging*, vol. 24, no. 2, pp. 439–443, Aug. 2006.
- [37] T. W. Redpath and J. M. Hutchison, "Estimating patient dielectric losses in NMR imagers," *Magn. Reson. Imaging*, vol. 2, no. 4, pp. 295–300, 1984.
- [38] J. G. van Heteren, R. M. Henkelman, and M. J. Bronskill, "Equivalent circuit for coil-patient interactions in magnetic resonance imaging," *Magn. Reson. Imaging*, vol. 5, no. 2, pp. 93–99, 1987.
- [39] L. S. Petropoulos and E. M. Haake, "Higher-order frequency dependence of radiofrequency penetration in planar, cylindrical, and spherical models," *J. Magn. Reson. 1969*, vol. 91, no. 3, pp. 466–474, Feb. 1991.
- [40] Y. Li, Y. Guo, and X. Jiang, "Signal-to-Noise Ratio Improvement by Bi-2223 Surface RF Coil in 0.3T MRI System," *IEEE Trans. Appl. Supercond.*, vol. 20, no. 3, pp. 818–821, Jun. 2010.
- [41] J. Wang, A. Reykowski, and J. Dickas, "Calculation of the signal-to-noise ratio for simple surface coils and arrays of coils [magnetic resonance imaging]," *IEEE Trans. Biomed. Eng.*, vol. 42, no. 9, pp. 908–917, Sep. 1995.
- [42] B. Cowan, *Nuclear Magnetic Resonance and Relaxation*. Cambridge: Cambridge University Press, 1997.
- [43] D. I. Hoult, "The NMR receiver: A description and analysis of design," *Prog. Nucl. Magn. Reson. Spectrosc.*, vol. 12, no. 1, pp. 41–77, 1978.
- [44] D. I. Hoult and R. E. Richards, "The signal-to-noise ratio of the nuclear magnetic resonance experiment," *J. Magn. Reson.*, vol. 213, no. 2, pp. 329–343, Dec. 2011.
- [45] A. Yahya, N. De Zanche, and P. S. Allen, "A dual-tuned transceive resonator for  $^{13}\text{C}\{^1\text{H}\}$  MRS: two open coils in one," *NMR Biomed.*, vol. 26, no. 5, pp. 533–541, May 2013.
- [46] D. Ahn, J.-H. Kweon, S. Kwon, J. Song, and S. Lee, "Representation of surface roughness in fused deposition modeling," *J. Mater. Process. Technol.*, vol. 209, no. 15–16, pp. 5593–5600, Aug. 2009.

- [47] I. Gibson, D. W. Rosen, and B. Stucker, *Additive Manufacturing Technologies*. NY, USA: Springer Science+Business Media, LLC, 2010.
- [48] C. R. Garcia, R. C. Rumpf, H. H. Tsang, and J. H. Barton, "Effects of extreme surface roughness on 3D printed horn antenna," *Electron. Lett.*, vol. 49, no. 12, pp. 734–736, Jun. 2013.
- [49] S. M. Gaytan, L. E. Murr, E. Martinez, J. L. Martinez, B. I. Machado, D. A. Ramirez, F. Medina, S. Collins, and R. B. Wicker, "Comparison of Microstructures and Mechanical Properties for Solid and Mesh Cobalt-Base Alloy Prototypes Fabricated by Electron Beam Melting," *Metall. Mater. Trans. A*, vol. 41, no. 12, pp. 3216–3227, Dec. 2010.
- [50] T. F. Pereira, M. A. C. Silva, M. F. Oliveira, I. A. Maia, J. V. L. Silva, M. F. Costa, and R. M. S. M. Thiré, "Effect of process parameters on the properties of selective laser sintered Poly(3-hydroxybutyrate) scaffolds for bone tissue engineering," *Virtual Phys. Prototyp.*, vol. 7, no. 4, pp. 275–285, Nov. 2012.
- [51] J.-W. Choi, F. Medina, C. Kim, D. Espalin, D. Rodriguez, B. Stucker, and R. Wicker, "Development of a mobile fused deposition modeling system with enhanced manufacturing flexibility," *J. Mater. Process. Technol.*, vol. 211, no. 3, pp. 424–432, Mar. 2011.
- [52] D. Mager, A. Peter, L. Del Tin, E. Fischer, P. J. Smith, J. Hennig, and J. G. Korvink, "An MRI Receiver Coil Produced by Inkjet Printing Directly on to a Flexible Substrate," *IEEE Trans. Med. Imaging*, vol. 29, no. 2, pp. 482–487, Feb. 2010.
- [53] S. Eosoly, D. Brabazon, S. Lohfeld, and L. Looney, "Selective laser sintering of hydroxyapatite/poly- $\epsilon$ -caprolactone scaffolds," *Acta Biomater.*, vol. 6, no. 7, pp. 2511–2517, Jul. 2010.
- [54] Arlon Materials for Electronics Division, "Electronic Substrates," *ARLON Technologies Enabling Innovation*. [Online]. Available: <http://www.arlon-med.com/index.cfm?fuseaction=portfolio.sub-category&portfolioCategoryID=76>. [Accessed: 18-Dec-2014].
- [55] "Specification - ROHACELL® - High-performance structural foam cores," *Evonik Industries*, 2010. [Online]. Available: <http://www.rohacell.com/product/rohacell/en/products-services/rohacell-hf/pages/default.aspx>. [Accessed: 18-Dec-2014].
- [56] M. Ahmadloo and P. Mousavi, "Application of novel integrated dielectric and conductive ink 3D printing technique for fabrication of conical spiral antennas," in *2013 IEEE Antennas and Propagation Society International Symposium (APSURSI)*, 2013, pp. 780–781.
- [57] A. Ranellucci, "Slic3r - G-code generator for 3D printers," *Slic3r, G-code generator for 3D printers*, 2011. [Online]. Available: <http://slic3r.org/>. [Accessed: 16-Dec-2014].
- [58] F. M. Smits, "Measurement of sheet resistivities with the four-point probe," *Bell Syst. Tech. J.*, vol. 37, no. 3, pp. 711–718, May 1958.
- [59] X. Zhang, K. Ugurbil, R. Sainati, and W. Chen, "An inverted-microstrip resonator for human head proton MR imaging at 7 tesla," *IEEE Trans. Biomed. Eng.*, vol. 52, no. 3, pp. 495–504, Mar. 2005.

- [60] J. Mispelter, M. Lupu, and A. Briguet, *NMR Probeheads for Biophysical and Biomedical Experiments: Theoretical Principles & Practical Guidelines*. Imperial College Press, 2006.
- [61] Q. X. Yang, S. Rupprecht, W. Luo, C. Sica, Z. Herse, J. Wang, Z. Cao, J. Vesek, M. T. Lanagan, G. Carluccio, Y.-C. Ryu, and C. M. Collins, “Radiofrequency field enhancement with high dielectric constant (HDC) pads in a receive array coil at 3.0T,” *J. Magn. Reson. Imaging*, vol. 38, no. 2, pp. 435–440, 2013.
- [62] T. Nakagawa, T. Nakiri, R. Hosoya, and Y. Tajitsu, “Electrical properties of biodegradable polylactic acid film,” in *Proceedings of the 7th International Conference on Properties and Applications of Dielectric Materials, 2003*, 2003, vol. 2, pp. 499–502 vol.2.
- [63] A. Ferrero, U. Pisani, and K. J. Kerwin, “A new implementation of a multiport automatic network analyzer,” *IEEE Trans. Microw. Theory Tech.*, vol. 40, no. 11, pp. 2078–2085, Nov. 1992.
- [64] H. Heuermann, “GSOLT: the calibration procedure for all multi-port vector network analyzers,” in *Microwave Symposium Digest, 2003 IEEE MTT-S International*, 2003, vol. 3, pp. 1815–1818 vol.3.
- [65] S.-J. Park and F.-L. Jin, “Synthesis and characterization of UV-curable acrylic resin containing fluorine groups,” *Polym. Int.*, vol. 54, no. 4, pp. 705–709, 2005.
- [66] F. D. Doty, G. Entzminger, J. Kulkarni, K. Pamarthy, and J. P. Staab, “Radio frequency coil technology for small-animal MRI,” *NMR Biomed.*, vol. 20, no. 3, pp. 304–325, 2007.
- [67] F. D. Doty, “Probe Design and Construction,” in *eMagRes*, John Wiley & Sons, Ltd, 2007.
- [68] J. Tropp, “Dissipation, resistance, and rational impedance matching for TEM and birdcage resonators,” *Concepts Magn. Reson.*, vol. 15, no. 2, pp. 177–188, Jun. 2002.
- [69] D. O. Brunner, N. De Zanche, “A symmetrically fed microstrip coil array for 7T,” *Proc. Intl. Soc. Mag. Reson. Med.*, vol. 15, p. 448, 2007.
- [70] P. Mansfield and P. G. Morris, *NMR imaging in biomedicine*. Academic Press, 1982.

## Appendix

### Slic3r Program and Settings:

A screenshot of Slic3r program is shown at Figure A-1. The plater tab Figure A-1-1 shows the projection of 3D model placed on the print-bed. In this window a model can be imported and the corresponding gcode can be exported. The type of filament and scaling factor can be selected. Rotate button can be used to rotate the model into the desired orientation. It is recommended to provide sufficient adhesion between first layer and print-bed. In this project, a layer of Kapton tape was laid on layer of double sided tape in order to maintain the adhesion. Print setting tab is shown Figure A-1-2, various settings for calculation of toolpaths and gcode output are given. The first layer height for plastic printing should be as high as possible, and additional layer height should be smaller for finer resolution.

The number of perimeters is the times extruder outlines the model for each layer and provides support for the infill. Layers can have a low infill density, such as empty, but first and top layer are completely filled for support. In infill section, the percentage of infill and the toolpath patterns can be selected. Depending on the model patterns such as rectilinear, concentric are the most suitable ones. The selection of speed is critical for a high quality print. Typically, for the first layer, the perimeter's speed is chosen to be low compared to infill speed for other layers. In output options, the ability of selecting verbose gcode is given, which gives many comments on gcode to follow the print step by step.

In tab of Figure A-2-1, settings of filament used and temperatures of extruder and print bed are set. The extruder and print-bed temperature for ABS is higher than PLA because of its higher melting temperature. Temperature greater than 75°C for the first layer of ABS allows good adhesion and lower temperature after the first layer should allow the layer to harden to the surface. For PLA, print-bed temperature of 60°C allows good adhesion. Figure A-2-2 includes print bed size and offset required for printing. Additionally, the gcode style or the required program for gcode is entered. Also second extrusion can be selected and its required information must be provided.

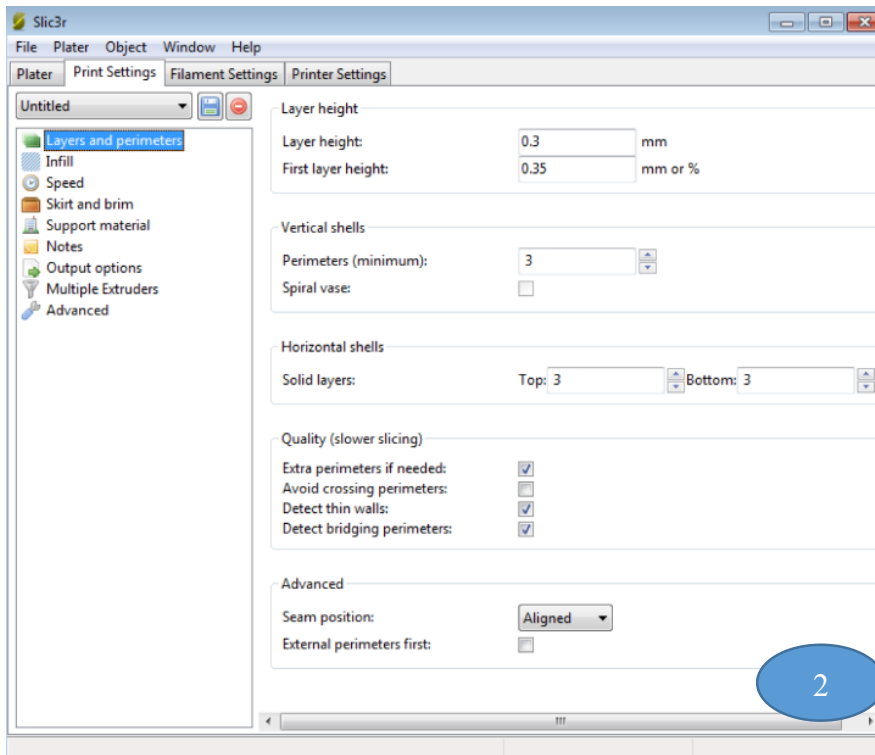
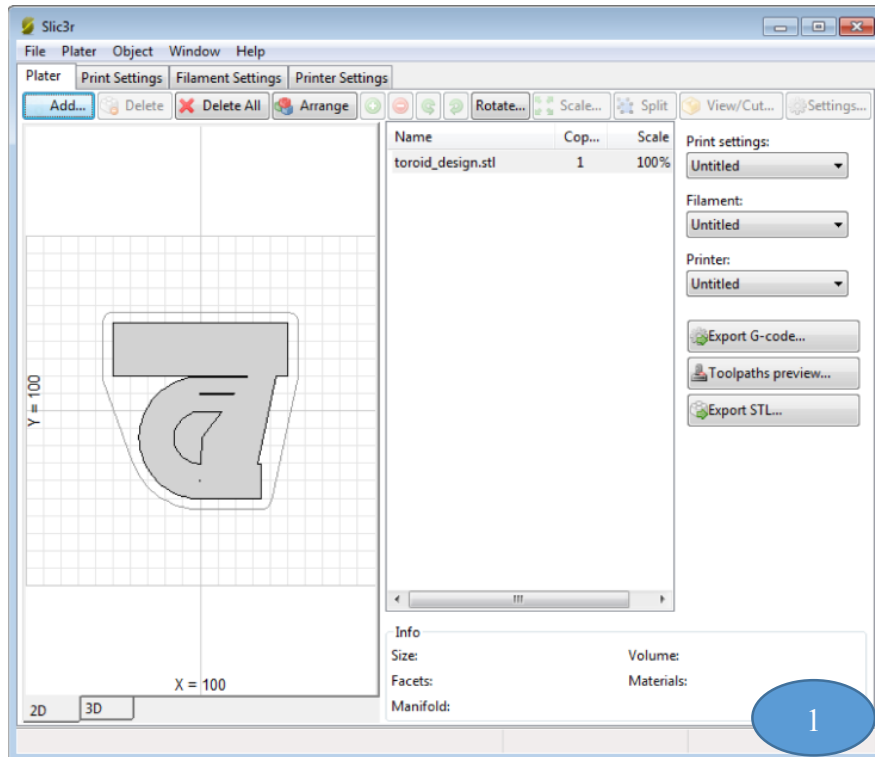


Figure A-1: Different tabs of Slic3r program 1: the plater, 2: the print settings.

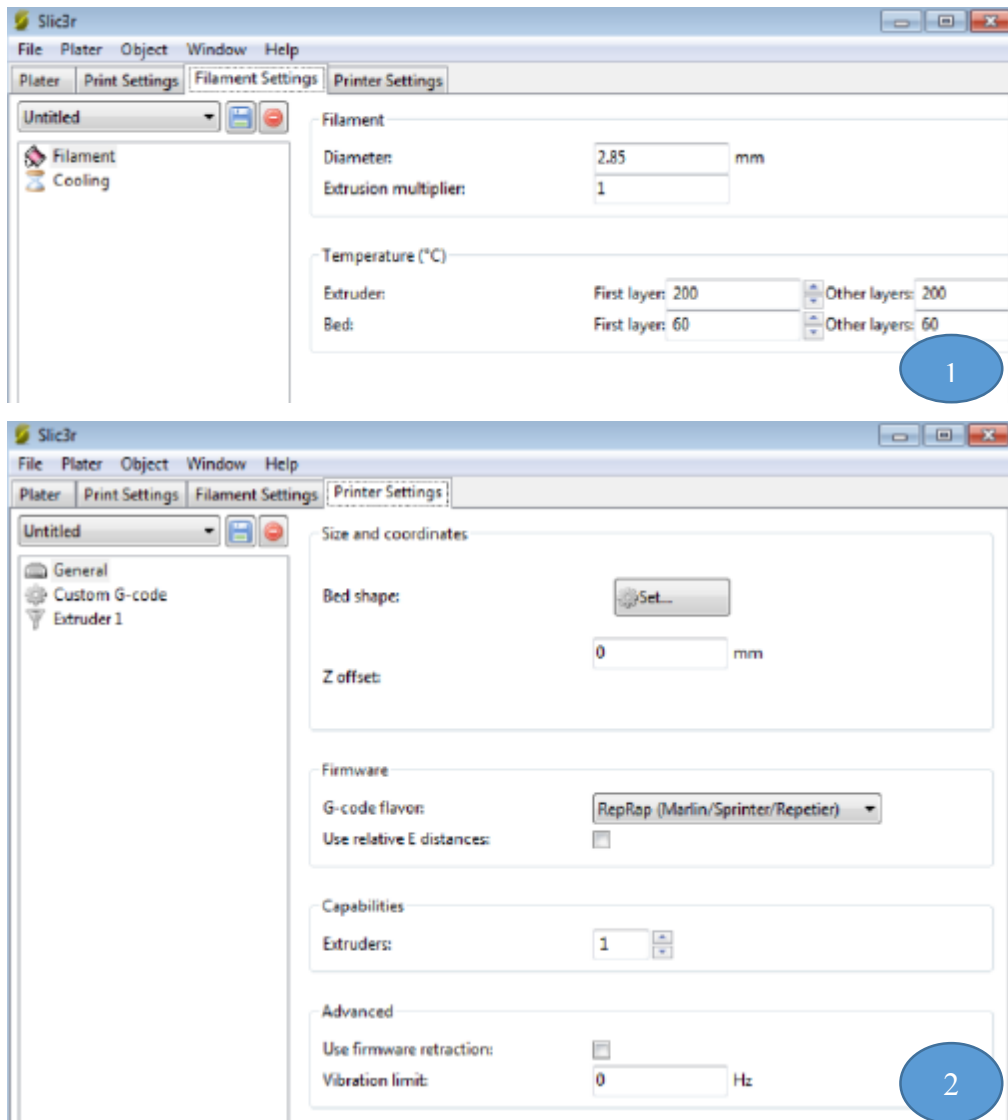


Figure A-2: Different tabs of Slic3r program 1: the filament setting, 2: the printer settings.

In Figure 4-3, gcode example of substrate printing is shown; comments at the end of each line represent what each comment means. There is usually a header indicating the settings that were used for Slic3r. After this, the settings for printing are given: units, temperature of extruder and print bed, and positioning. Before printing, the axis is moved to zero to initialize the printing because printer doesn't know the location of extruder at the beginning. Instruction for printing comes next; it involves raising the extruder to the height of each layer first. The printing begins by making a print outline or as it is called a skirt in Slic3r, and then the perimeter of each layer.

Printing ends with turning of the extruder and print-bed's temperature and homes all axes. The modification for ink printing mainly involves adding an offset to gcode to take into account the location of the syringe compared to the extruder. This also involves modifying the speed for ink printing.

### **Model Exporting and Ink Printing:**

HFSS is used to simulate and create 3D models. A CAD exchange software can be used to convert the HFSS file to .stl file. The ink must be separate from plastic/substrate layer. The model should be oriented in the orientation that the model is desired to be printed or how it is required to be for the ink printing. The ink printing process starts with Figure 4-5, red sections represent the ink and green sections are substrate. The ink layer height is set to 0.2mm which is the single layer height that will be set in slic3r to print ink, and then gcode can be exported. The modifications for gcode are shown in Figure 4-6. The infill density for ink layer must be set to some low value depending on the ink.

For this process an infill density of 45% is chosen for ink layer. A much lower infill density can result in separated printed lines from each other, on the other hand a bigger value will result in thicker layer. Speed of 10mm/s is used for layers, which is significantly slower than normal plastic extrusion speed. A layer similar to substrate layer for the top and bottom plates, and the signal line can be modeled with 0.2mm thickness. One important consideration in layer geometry is that layer of ink can be slightly smaller in the edges to avoid spill of ink from edges. The height of extruder must be raised according to the height of targeted layer, it is important to avoid contact between ink and extruder. Two commands are used to raise the extruder which are F9000, and F40. F9000 works well for small distances and F40 works for long distances in z direction.

The syringe must be placed lower than the tip of extruder to avoid contact between ink and extruder. Home coordinates of the substrate and the skirt that the substrate is printed inside can help us to find the starting point for substrate layer, and by adding the offsets for syringe ink printing can be started. A command

“@pause” can be inserted at the first ink line in order to observe if there is any misalignment.

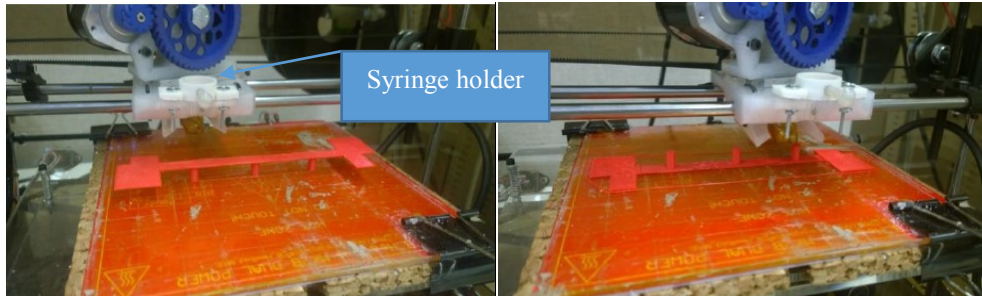


Figure A-3: The resonator shown flipped (left) and in the printing orientation (right). The skirt is printed around in both cases so the resonator can be positioned accurately for ink or additional layer printing.

The “skirt” helps to position the resonators correctly for ink printing. As it can be seen in Figure A-3-right, syringe must be raised to height of first layer of substrate, then ink can be printed on the bottom plates of capacitors. The bed temperature maintains adhesion for PLA when ink is being printed on it. For signal line and top plates, the extruder should be raised to the required height using the F40 command. In the table the critical parameters that were used in ink printing process are listed.

Table A-1: Ink-process parameter settings

<i>Parameter name</i>	<i>Recommended values</i>
<i>Speed</i>	10mm/s
<i>Infill</i>	40-45%
<i>Infill pattern</i>	Rectilinear
<i>Layer thickness</i>	0.2mm
<i>Bed temperature</i>	ABS=80°C, PLA=60°C

### **Offset Measurement:**

In order to measure the offset between syringe and extruder, a method was adopted as explained here. A paper is placed on the print bed. The tip of the syringe is dipped into small amount of red ink. The extruder temperature is set to 220°C manually in RepetierHost. After fixing the syringe location, both extruder and

syringe are brought down to make signs on the paper. With this method, x and y offsets are calculated.